

Data Recovery from Magnetic Media Using Magnetic Force Microscopy

by

Terry R. Ferrett

Thesis submitted to the
College of Engineering and Mineral Resources
at West Virginia University
in partial fulfillment of the requirements
for the degree of

Master of Science
in
Electrical Engineering

Matthew C. Valenti, Ph.D., Chair
Natalia Schmid, Ph.D.
Charter D. Stinespring, Ph.D.
Andrew A. Woodworth, Ph.D.

Lane Department of Computer Science and Electrical Engineering

Morgantown, West Virginia
2008

Keywords: Magnetic Force Microscopy, Magnetic Recording Channel, Fourier Analysis,
Data Recovery

Copyright 2008 Terry R. Ferrett

Abstract

Data Recovery from Magnetic Media Using Magnetic Force Microscopy

by

Terry R. Ferrett

Master of Science in Electrical Engineering

West Virginia University

Matthew C. Valenti, Ph.D., Chair

Magnetic tapes are widely used to store voice and other data. Due to the effect of hysteresis, modification of the magnetization pattern written to a tape by overwriting, erasing, or physical damage leaves remanent information about the previous magnetization state that can not be discerned by standard audio playback devices. Recently, a high resolution microscopy technique known as magnetoresistive microscopy was used by Pappas et. al. in an attempt to recover data from audio tapes which were physically damaged. However, the device, while having a higher resolution than tape playback heads, still averages over entire audio track widths when collecting data. The purpose of this thesis is to propose and investigate a methodology for the recovery of erased data using a microscopy technique known as magnetic force microscopy (MFM). This is a novel approach because MFM can achieve much higher resolution than previous techniques, on the order of nanometers. The primary analysis technique utilized is the fast Fourier transform, which is applied to MFM images of strongly written, weakly written, and erased sinusoidal tones recorded by a standard audio tape deck. To verify our data collection and pre-processing techniques, a numerical simulation of tape media and MFM response is presented and compared with measurement. Several processing techniques, such as windowing to reduce FFT spectral leakage, thresholding to remove the effects of destructive magnetic interference, and tip response deconvolution to remove instrument dependent features from the data, are applied. It was found that at certain frequencies recovery of tones after erasure is possible, suggesting that erasure is frequency dependent. By investigating and altering audio tape samples *in situ*, the same physical section of tape was imaged several times, and it was found that the erasure process varies with position, even down to the order of microns.

To my mother and father, whose patience, support, encouragement, and love have taught me that anything is possible with enough dedication and desire. To my wonderful sister Jenny for her friendship, faith, love, and her inspiring devotion as both a scholar and a mother. To my great sister Kristen for her unending love and support. Words cannot express the gratitude I have towards my entire family, who made this work and all of my achievements possible. To them, I dedicate this thesis.

Acknowledgments

This work is truly a collaboration of many different viewpoints and disciplines, and without the support provided by my advisor, my committee, and my friends it would not have been possible. The guidance, careful attention to quality and detail, and technical advice given by my advisor Dr. Matthew C. Valenti were invaluable. Dr. Valenti is a wonderful advisor and a great friend. Dr. Charter Stinespring and Dr. Natalia Schmid were very gracious to serve on my committee and their technical expertise proved both helpful and inspiring. A special thanks goes to Dr. Andrew Woodworth, who made many sacrifices on my behalf to make this work possible. The long hours Dr. Woodworth spent mentoring me, gathering and analyzing the data in this work, and the technical advice he imparted upon me are greatly appreciated and will not be forgotten. Dr. Rohit Iyer Seshadri deserves special thanks for his friendship, mentoring, and advice, both technical and personal. Last but most certainly not least, a thanks to everyone in the Wireless Communications Research Laboratory and the Surface Sciences Laboratory for their dedication, support and friendship.

Contents

Acknowledgments	iv
List of Figures	viii
List of Tables	x
Notation	xi
1 Introduction	1
1.1 Motivation and Objectives	1
1.2 Thesis Outline	3
2 Magnetic Recording Overview	5
2.1 The Magnetic Recording Channel	5
2.1.1 Basic Principles of Magnetism	5
2.1.2 Recording Heads	9
2.1.3 Media	10
2.2 Recording and Reproduction	13
2.2.1 Magnetization Patterns	13
2.2.2 Ring Head Reproduction	15
2.3 Noise	17
2.3.1 Noise Theory	17
2.3.2 Noise Overview	20
3 Magnetic Force Microscopy Principles of Operation	22
3.1 An Overview of MFM	22
3.1.1 Scanning Probe Microscopy	23
3.1.2 MFM Subsystems	23
3.1.3 A Mathematical Model of MFM	25
3.2 Magnetization Estimation using MFM Images	28
3.2.1 Magnetization Estimation through Tip Response Function	28
3.2.2 Simulated MFM Images	31
3.2.3 Data Comparison	35

4	Analysis of Noise and Erasure	37
4.1	Erasibility and Overwrite of Media	37
4.1.1	Erasure Techniques and Overwrite	38
4.1.2	Partial Erasure	39
4.1.3	Noise Analysis	44
4.2	Data Recovery	49
4.2.1	Single Tone Data	49
4.2.2	Multi-tone Data	54
4.2.3	<i>In situ</i> Erased Data	60
5	Conclusion	70
5.1	Summary and Conclusions	70
5.2	Future Work	71
	References	73
A	Analysis Techniques Applied to MFM Data	76



List of Figures

2.1	Bar magnet.	7
2.2	Hysteresis loop.	8
2.3	Inductive ring head.	9
2.4	Scanning electron microscope image of audio tape surface.	12
2.5	Field distribution near gap.	13
2.6	Write head near gap - two transitions. N denotes magnetic north and S denotes magnetic south. TZ denotes transition zone.	14
2.7	Write head near gap - several transitions. N denotes magnetic north and S denotes magnetic south. TZ denotes transition zone.	15
2.8	Anhyysteretic magnetization curve. The y axis represents the remanent magnetization, while the x axis represents a constant magnetizing field added to a decaying cyclic field.	15
2.9	Ring head reproduction.	16
2.10	Row of magnetized particles. [1]	18
3.1	(a) Block diagram of magnetic force microscope and (b) diagram of coordinate system in the vicinity of the MFM tip.	24
3.2	Simulated MFM response to audio recording media showing magnetic transitions. Normalization constants are $723 \text{ Oe}(H)$ and $3.28 * 10^{15} \text{ N}/\mu\text{m}(F/m)$	28
3.3	Simulated dipole response function.	30
3.4	Particle model used to generate magnetization patterns.	32
3.5	Single magnetic dipole (a) shown with a simulated MFM image of seven dipoles (b).	33
3.6	Simulated magnetization map of a cross-section of the particle model. Image (a) is the original and image (b) is the recovered image.	34
3.7	MFM image of a noisy audio recording vs a simulated MFM image of a noisy magnetic field map.	35
3.8	Comparison of MFM images to simulation - single tone.	36
3.9	Comparison of MFM images to simulation - multiple tones.	36
4.1	Partial erasure images - erased area.	41
4.2	Partial erasure images - partially erased area.	42
4.3	Partial erasure images - strong signal area.	43
4.4	Comparison of theoretical and measured noise statistics - strong signal 1. . .	45

4.5	Comparison of theoretical and measured noise statistics - strong signal 2. . .	45
4.6	Comparison of theoretical and measured noise statistics - weak signal 1. . . .	47
4.7	Comparison of theoretical and measured noise statistics - weak signal 2. . . .	47
4.8	Image of audio tape layout showing the locations from which MFM data was taken. The top track is written with a 2 kHz sine wave. The bottom track was written with the same wave and then erased.	50
4.9	Area A - Top of unerased track - Image 1.	51
4.10	Area A - Top of unerased track - Image 2.	52
4.11	Area C - Top of erased track - Image 1.	52
4.12	Area C - Top of erased track - Image 2.	53
4.13	Area D - Bottom of erased track - Image 1.	53
4.14	Area D - Bottom of erased track - Image 2.	54
4.15	Image of audio tape layout showing the locations from which MFM data was taken. The bottom track is written with a 5 kHz and a 14 kHz sine wave. The top track was written with the same waves and then erased.	56
4.16	Area G - Bottom of unerased track - Image 1.	56
4.17	Area G - Bottom of unerased track - Image 2.	57
4.18	Area A - Top of erased track - Image 1.	57
4.19	Area A - Top of erased track - Image 2.	58
4.20	Area B - Top of erased track - Image 1.	58
4.21	Area B - Top of erased track - Image 2.	59
4.22	Area H - Buffer area - Image 1.	59
4.23	Area H - Buffer area - Image 2.	60
4.24	10 kHz wave $25 \times 25 \mu m$ - Unaltered signal - Image 1.	62
4.25	10 kHz wave $25 \times 25 \mu m$ - Unaltered signal - Image 2.	62
4.26	10 kHz wave $25 \times 25 \mu m$ - First altered signal - Image 1.	63
4.27	10 kHz wave $25 \times 25 \mu m$ - First altered signal - Image 2.	63
4.28	10 kHz wave $25 \times 25 \mu m$ - Second altered signal - Image 1.	64
4.29	10 kHz wave $25 \times 25 \mu m$ - Second altered signal - Image 2.	64
4.30	10 kHz wave $90 \times 90 \mu m$ - Unaltered signal - Image 1.	65
4.31	10 kHz wave $90 \times 90 \mu m$ - Unaltered signal - Image 2.	65
4.32	10 kHz wave $90 \times 90 \mu m$ - Altered signal - Image 1.	66
4.33	10 kHz wave $90 \times 90 \mu m$ - Altered signal - Image 2.	66
4.34	Image showing the correlation between segments of Fig. 4.24(a) and Fig. 4.26(a).	67
4.35	Image showing the correlation between segments of Fig. 4.24(a) and Fig. 4.28(a).	68
4.36	Image showing the correlation between segments of Fig. 4.30(a) and Fig. 4.32(a).	69
.1	Child on a swing.	76
.2	Swing time and frequency data.	76
.3	Swing data truncated after a non-integer number of periods.	79
.4	Kaiser-Bessel window applied to swing data in Fig. .3	80
.5	Flat top window applied to swing data in Fig. .3	80

List of Tables

2.1	Magnetic material used in media [2], saturation remanence M_r , coercivity H_c , and average number of particles per unit volume, N , of various types of particulate magnetic recording media. The unit “emu” is an abbreviation for “electromagnetic unit” and is defined as 4π micro-oersteds. The oersted is the CGS unit of magnetic field strength.	12
3.1	Parameters for MFM response simulation.	28
4.1	Summary of Signal-to-Noise ratios for the single-tone data set.	51
4.2	Summary of Signal-to-Noise ratios for the multi-tone data set.	60
4.3	Summary of Signal-to-Noise ratios for the electromagnet-altered data set. . .	61

Notation

We use the following notation and symbols throughout this thesis.

$\vec{\mu}$: Magnetic dipole moment
μ	: Magnetic permeability
\vec{B}	: Magnetic induction
\vec{H}	: Magnetic field strength
\vec{M}	: Magnetization
ϕ	: Flux density
σ^2	: Variance
$\nabla(\cdot)$: Gradient
$\mathcal{F}(\cdot)$: Fourier Transform
$\mathcal{F}^{-1}(\cdot)$: Inverse Fourier Transform

Chapter 1

Introduction

1.1 Motivation and Objectives

Audio cassette tapes are used to store a wide variety of data. The use of these tapes for dictation, music storage, etc, has led to a great volume of data stored in magnetic form. The use of audio cassettes has declined in recent years with the advent of compact disks and digital voice recorders, but audio cassettes remain a niche market for applications such as voice recording for taking notes, and recording police interviews, which for police interrogations in the UK is mandatory [3]. In many ways magnetically stored data is more volatile than data stored in other common formats, such as compact discs and flash memory drives [2]. Magnetically stored data is subject to degradation over time and corruption from exposure to unwanted magnetic fields, such as the Earth's magnetic field, or deliberate erasure by recording devices. Perhaps the most high profile example of deliberate erasure is the fifteen minute gap on a tape-recorded conversation between former President Richard M. Nixon and his chief of staff, H. R. Haldeman on June 20th, 1972. This gap was allegedly deliberately created by Nixon's secretary, Rose Mary Woods, and has yet to be recovered by any known forensic technology [4].

Retrieval of corrupted magnetic data has thus far been performed primarily by low resolution methods, such as the actual audio playback heads in the cassette decks themselves [5]. Recovering data from tape using the tape deck itself is not optimal because the playback head averages over large sections of media, approximately $2 \mu m^2$. The retrieval technique

utilized in this thesis, *magnetic force microscopy* (MFM), exhibits resolving power on the order of tens to hundreds of nanometers [6]. This provides a unique opportunity to investigate erased media for useful information previously inaccessible by other techniques. Also, this high resolution allows experimental verification of theoretical predictions of magnetic behavior, such as media noise at the particle level, which are not observable using low resolution techniques.

This thesis proposes and investigates an approach to recovering data from erased audio cassette tapes using MFM. To our knowledge, no previous attempts to recover erased data using MFM have been published. Pappas et. al. [7] were able to recover data from physically damaged audio tapes using magnetoresistive microscopy, but the data in this case was not erased, as this work was primarily aimed at forensic investigation. Remanent data from misregistration of write heads in digital media has been investigated by Gomez et. al. [8], and imaging of overwritten data was performed by Mayergoyz et. al. [9], but no explicit attempts have been made to recover erased data using MFM. The primary numerical tool used to investigate the data is the fast Fourier transform (FFT). This decision was made because the studied data consists of single and multiple sinusoidal tones recorded to and erased from audio tapes, and the FFT provides a convenient representation of the sinusoidal spectrum of the data. Several processing techniques are applied to the data in an attempt to increase the signal-to-noise ratio (SNR) in the computed FFT's. These include the application of a deconvolution function, referred to in this context as a tip response function, to remove the MFM-specific imaging artifacts from the measured data [10]. Another processing technique applied to the data is the identification and reversal of destructive magnetic interference at the particle level, referred to as partial erasure [11].

Further investigations include fitting a statistical model of audio tape media noise to observed data, and the creation of a simple numerical simulation of tape media and MFM response for verification against experimental data. There are two main goals in studying noise. The primary goal is to develop robust signal recovery methods which make use of all available information in the presence of noise. The second is to understand what fundamental limitations exist in our ability to resolve weak signals from MFM data. Media noise can roughly be considered additive, white and Gaussian (AWGN) in nature, and inhibits the

recovery of a signal much as AWGN corrupts the signals transmitted in a wireless communication system. No known work has attempted to verify noise models using a device with resolution as high as MFM. An overview of other studies performed on noise is also presented. It is hoped that this work motivates the development of an optimal signal detector for magnetic recording channels in a similar vein as the matched filter, which is the optimum linear detector for the AWGN channel.

1.2 Thesis Outline

The objective of this thesis is to investigate techniques for recovering erased data from audio tape using MFM. To reach this objective, the thesis covers the following topics. Chapter 2 introduces basic principles of magnetism, including terminology, magnetic recording heads, and properties of tape media. Concepts are presented such as the quantification of magnetization, magnetic fields and a basic discussion of ferromagnetic materials. Simplified magnetization patterns observed in recording media are shown. The chapter concludes by introducing a theory of noise which is compared with experimental data in a later chapter, followed by a literature review discussing ways in which the noise theory could be extended to form a more complete model.

Chapter 3 introduces the concepts underlying MFM, including a basic discussion of the underlying physics, and a block diagram. A brief overview of scanning probe microscopy (SPM), the technique from which MFM is derived, is presented, along with a mathematical model of the magnetic interactions present in the MFM measurements. From this a simple one-dimensional simulation of MFM response is developed to illustrate key operating concepts and motivate the extension into three dimensions. A discussion of the tip response function, its application to data, and its implementation in Fourier space is presented. Finally, simulated MFM images from the three-dimensional tape model are shown and compared to actual MFM data.

Chapter 4 presents the results of analysis, including FFT data of an assortment of MFM images both erased and unerased, and comparison of the noise model discussed in chapter 2 with experiment. The phenomenon of partial erasure is discussed and analyzed. Single-tone

recorded data and multi-tone recorded data are investigated after erasure. Additionally, samples which are erased while in the MFM sample tray (*in situ*) are investigated. These samples are interesting because they allow the exact same physical area to be imaged multiple times, which is difficult if not impossible when moving samples into and out of the MFM. Chapter 5 summarizes the results, presents conclusions, and makes suggestions for future work.

Chapter 2

Magnetic Recording Overview

This chapter provides an introduction to the concepts behind magnetic recording. First, a discussion of the recording channel is presented, including magnetic principles, read/write heads and media properties. Next, reproduction of the recorded signal is considered. Finally, the origin of noise and interference is discussed.

2.1 The Magnetic Recording Channel

This section introduces terminology and concepts that are used throughout the thesis. Basic magnetic concepts are covered, such as the source of magnetic fields, field strength, dipole moments, and the quantification of magnetization. A discussion of the nonlinear properties of magnetization and a technique for linearization is presented. Also, recording heads and their magnetic properties are presented, followed by a treatment of common recording media.

2.1.1 Basic Principles of Magnetism

Magnetic fields arise from the flow of electric current. This can either be a macroscopic current in a length of wire, or the current arising from an intrinsic property of electrons called *spin*. In most materials, these electron spins occur in pairs which cancel each other's magnetic fields. However, in materials with unpaired electron spins, net magnetic fields which are detectable outside the material arise. The product of current and the area enclosed by

the loop in which it flows is called the *magnetic dipole moment* and is expressed as [12]:

$$\vec{\mu} = I\pi r^2 \quad (2.1)$$

where I is the current and πr^2 represents the area enclosed by the loop. Current is typically measured in amperes (A), while distance is measured in meters (m).

Magnetic dipole moments can be visualized by imagining a permanent bar magnet, as shown in Fig. 2.1. The field lines around the magnet represent the *magnetic induction*, denoted by \vec{B} , and having units newtons per ampere-meter [$N/(Am)$], or *teslas*. Magnetic induction at a particular point is a measure of the force experienced by an electric current-carrying conductor at that point. The spacing of the field lines (their *density*) is used to represent relative values of \vec{B} in space, which are a function of the material in which the field is propagating and the distance from the magnetic source. The magnitude of the magnetic flux density drops in proportion to the inverse square of the distance from the source. An unambiguous description of the external field, irrespective of the medium of propagation, is given by the *magnetic field strength*, \vec{H} , which is related to magnetic flux density by the relationship:

$$\vec{B} = \mu \vec{H} \quad (2.2)$$

where \vec{H} has units of *amperes/meter* and μ is the *permeability* of the medium. Since flux density \vec{B} is linearly related to permeability, the two quantities are analogous to electrical current and conductivity. The permeability can be expressed as: $\mu = \mu_0 \mu_r$, where μ_0 is the *permeability of free space* with units tesla-meters per ampere (Tm/A), and μ_r is the *relative permeability*, a dimensionless ratio. For example, iron has a relative permeability of $\mu_r = 200$. So, a magnetic field with strength \vec{H} propagating in iron would generate flux with density:

$$\vec{B} = 200\mu_0 \vec{H}. \quad (2.3)$$

The magnetic materials used for recording are classified as *ferromagnetic*. Ferromagnetic materials retain a magnetization proportional to the applied \vec{B} field, even after the field is

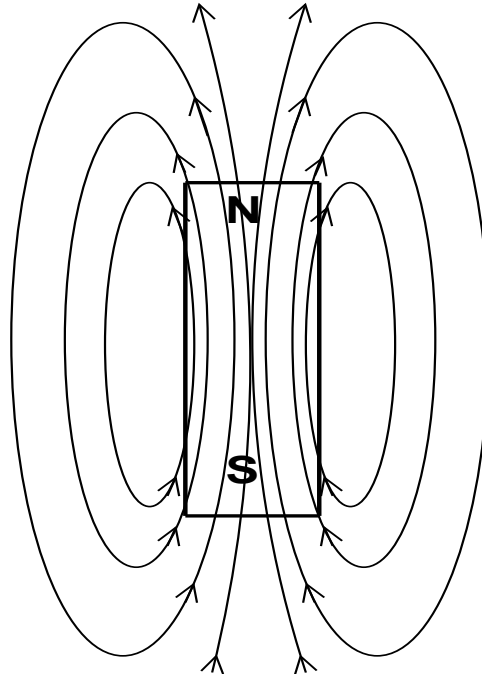


Figure 2.1: Bar magnet.

removed. Magnetization is expressed in terms of net magnetic moment per unit volume of the material, $\vec{M} = \vec{\mu}/m^3$. \vec{M} has units amperes per meter (A/m). Examples of ferromagnetic materials are iron, cobalt, and nickel. Ferromagnetic materials contain multiple large regions, called *domains*, within which the moments are aligned with each other. This alignment allows ferromagnetic materials to exhibit net magnetizations, even when no external \vec{B} fields are present.

The relationship between the net magnetization of a material and the externally applied field is illustrated in Fig. 2.2. Observing this graph reveals that the relationship is nonlinear and has memory, so that the response to an arbitrary field is a function of the material's previous magnetization state. The loop in this figure is known as the *major hysteresis loop*. Point 1 denotes the beginning of the initial magnetization curve, where the magnetization of the material and the external field are both zero. If we begin at 1 and slowly apply an increasing external field, the material's magnetization will traverse along this initial magnetization curve to point 2, known as the *saturation magnetization*, \vec{M}_s . This is the magnetization at which all the domains in the material are aligned in the same direction, and magnetization is

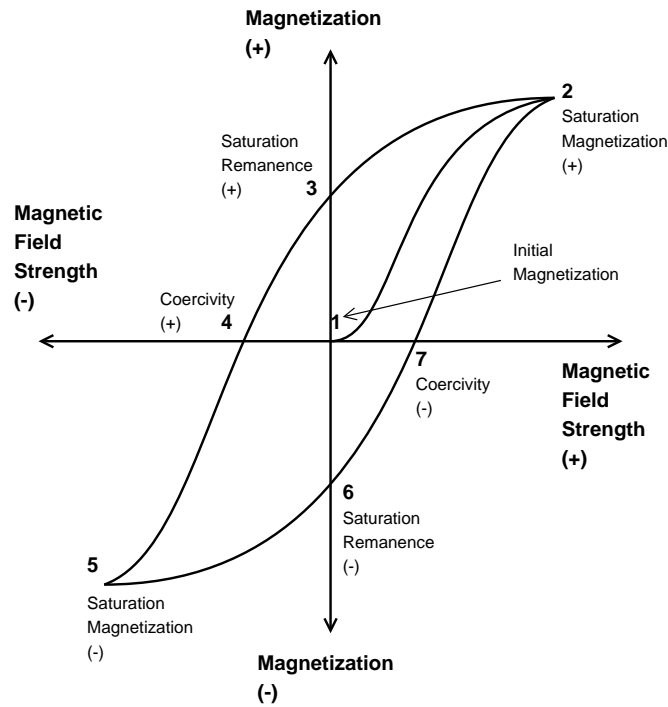


Figure 2.2: Hysteresis loop.

maximized. No matter how much more the external field is increased, the magnetization of the material will not exceed saturation. If we then begin decreasing the magnetic field back towards zero, the material's magnetization will follow the curve from 2 to 3. The point 3 on the graph shows the *remanent magnetization*, \vec{M}_r . This is the magnetization which remains after the externally applied field falls to zero. \vec{M}_r is smaller than the saturation magnetization since some of the domains fall out of alignment after the external field is removed. It is this remanent behavior that causes ferromagnetic materials to exhibit memory.

Let us now reverse the polarity of the applied field and begin increasing it in the opposite direction. This will take us from point 3 to point 4, the coercivity \vec{H}_c of the material. \vec{H}_c is the applied field necessary to bring the magnetization of the material down to zero after having been driven to saturation. We can then proceed around the curve from 4 to 5 and eventually back to 2 again, by applying an oscillating external field. However, we can never return to point 1 by traversing the major hysteresis loop. Returning to the initial magnetization point is achieved by a technique called *biasing*, which is discussed in Section 2.2.1.

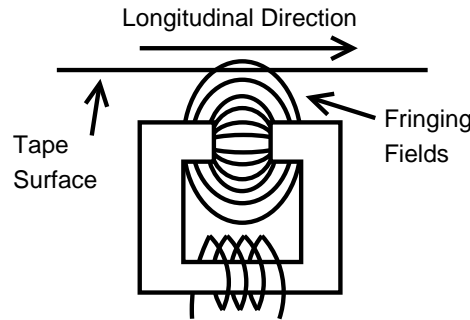


Figure 2.3: Inductive ring head.

2.1.2 Recording Heads

The conversion of signal voltages and currents to magnetic fields is achieved in the recording head. Heads are therefore the primary transducers in a magnetic recording circuit. Depending on the application, distinct heads can be used for recording, playback, and erasure, or the same head can be used for all functions. In the case of audio recording, high quality tape recorders utilize separate heads for all functions, while average quality devices combine the record and playback functions into one head. Some lower quality devices combine all three functionalities into the same head. These different configurations of heads have an effect on the overwrite characteristics of audio recordings.

The most common type of recording head is the inductive ring head, shown in Fig. 2.3. This head consists of a toroid with small section removed, allowing magnetic flux to fringe outward and into the recording media. This type of head creates a magnetizing field primarily in the longitudinal (along the track) direction.

Physical distinctions exist between record, playback, and erase heads. The gap in the recording head is designed so that sufficient induction is generated to magnetize the recording medium, while decreasing quickly along the direction of the track so that short wavelength signals are not distorted. Typical record head gap lengths range from 2.5 to 12 microns. Playback heads are similar in construction to record heads, but typically have more windings and cores with higher permeability to increase flux density. Playback heads have the smallest gap lengths, on the order of 1.5-6 microns. Erase heads do not have as strict requirements for spatial resolution, and use high field amplitudes, so their design is the least critical [2].

Permanent magnets and DC excited heads can be used for erasing, but these produce higher noise in the media than an AC-excited head. These typically have gap length between 25-125 microns.

A summary of the magnetic characteristics of inductive heads is given below [2]:

1. **Permeability** $\mu = \mu_r \mu_0$, the ratio of magnetic induction B to field H , is a key parameter for read and write performance. It defines the range of magnetization over which a given range of signal values is mapped, and so describes the resolution of recording.
2. **Saturation magnetic induction** \vec{B}_s dictates the maximum flux density which can be obtained in the head. This is limited by the maximum write current in the head and the saturation magnetization of the core.
3. **Coercivity** \vec{H}_c is the field necessary to reverse the magnetization and decrease the magnetic induction of the *head* (not the medium) to zero. It is a measure of the ease of switching the magnetization of the head.
4. **Remanent magnetic induction** \vec{B}_r is the magnetic induction remaining around the head with zero applied field. Its value is closely related to coercivity and permeability and controls the residual field in and around the head, after magnetization during writing has ceased. After head current has been reduced to zero, some magnetization is always left over in the head material, leading to finite magnetic induction.

2.1.3 Media

The basis of magnetic recording is in the magnetization of ferromagnetic materials which form a history of the input signal. Analog audio recording is dominated by a form of media known as *particulate media*. Particulate media is formed by depositing small magnetic particles onto a nonmagnetic substrate. This design allows for independent optimization of the substrate layer and the magnetic layer [2]. As a result of this property, a strict international standard for the manufacture of audio recording tapes has been established.

Recording characteristics of particulate media are determined by the type of magnetic layer used, its physical configuration, and the shape of the particles. The most common material used for the creation of magnetic particles is gamma ferric oxide. A summary of the magnetic properties of this and other materials used in the magnetic recording layer is given in Table 2.1. The signal-to-noise ratio (SNR) is primarily determined by the saturation remanance \vec{M}_r , defined as the remanent magnetization after the media is driven to saturation, and the coercivity \vec{H}_c . As these values increase, so does the SNR. High quality home recording decks exhibit SNR's on the order of 70 dB. The wavelength of the recorded signal determines the depth to which it is recorded [2]. Higher frequencies are recorded primarily in the first 1 to 2 μm of tape depth, and the coercivity of this depth is typically 1.5 times that of the regions below it, from 2-5 μm . The particles in audio tapes are needle-shaped and are oriented predominantly in the down-track direction. This physical configuration favors magnetization in the longitudinal direction, which helps reduce cross-track interference. The size of each individual particle is on the order of 0.1 - 1.5 μm . A scanning electron microscope image of magnetic tape particles is shown in Fig. 2.4. From specifications of the dimensions and operating characteristics of audio tape, we can calculate the number of particles affected by different wavelengths. At the upper end of audio cassette frequency response, 20 kHz, the wavelength of one period is given by:

$$\frac{47.5 \text{ mm/s}}{20 \text{ kHz}} = 18 \mu m \quad (2.4)$$

where 47.5 mm/s is the speed of the tape [13]. Using the statistics for Audio tape IEC II in Table 2.1 with particle density per unit volume $N = 1.4 \times 10^3/\mu m^3$, the average number of particles magnetized per unit wavelength at this frequency is:

$$600 \mu m \times 5 \mu m \times 18 \mu m \times N = 54 \times 10^3 \text{ particles} \quad (2.5)$$

where 600 μm is the width of a stereo track, 5 μm is the depth of the magnetic material and 18 μm is the length of tape recorded.

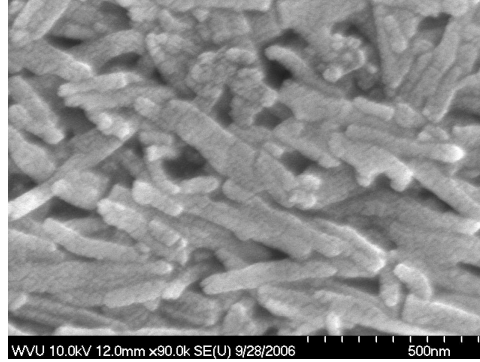


Figure 2.4: Scanning electron microscope image of audio tape surface.

Application	Material	M_r , kA/m , (emu/cm^3)	H_c , kA/m , ($4\pi Oe$)	N , $10^3/\mu m^3$
Reel-to-reel audio tape	$\gamma - Fe_2O_3$	100-120	23-28	0.3
Audio tape IEC I	$\gamma - Fe_2O_3$	120-140	27-32	0.6
Audio tape IEC II	CrO_2	120-140	38-42	1.4
	$\gamma - Fe_2O_3 + Co$	120-140	45-52	0.6
Audio tape IEC IV	Fe	230-260	80-95	3
Professional video tape	Fe	240	110-125	4
	CrO_2	110	42	1.5
	$\gamma - Fe_2O_3 + Co$	90	52	1
Home video tape	CrO_2	110	44-58	2
	$\gamma - Fe_2O_3 + Co$	105	52-74	2
	Fe	220	110-125	4

Table 2.1: Magnetic material used in media [2], saturation remanence M_r , coercivity H_c , and average number of particles per unit volume, N , of various types of particulate magnetic recording media. The unit “emu” is an abbreviation for “electromagnetic unit” and is defined as 4π micro-oersteds. The oersted is the CGS unit of magnetic field strength.

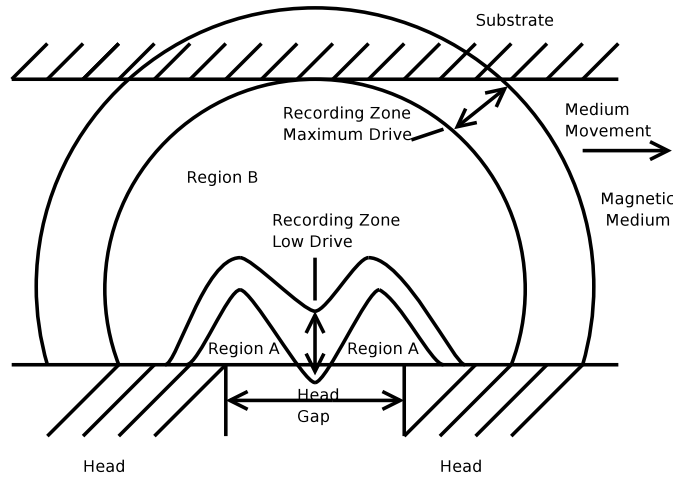


Figure 2.5: Field distribution near gap.

2.2 Recording and Reproduction

This section gives an example of a recorded section of media, and shows how the magnetized regions correspond to the different regions of flux from the write head. This provides physical insight into the magnetization of media by the write head. A technique for linearizing magnetic hysteresis behavior is presented. Magnetic ring head reproduction is discussed briefly, and an ideal relationship for ring head reproduction is given.

2.2.1 Magnetization Patterns

An illustration of ideal magnetization patterns provides insight into interpreting data presented in later sections. In this section, we will observe effects of magnetization on a small segment of tape, and discuss the different regions of magnetization within the tape thickness. Anhyseretic magnetization is contrasted with the hysteretic phenomenon discussed in section 2.1.1.

A field is generated in the gap of a write head when the write head coil is energized. This field fringes out from the gap and into the media, as shown in Fig. 2.5 [14]. The maximum magnetizing field occurs in region A and the region marked “Recording Zone Maximum Drive”. The field in the maximum drive region contributes the most to the remanent magnetization in the media. Region A and the maximum drive region are separated

from one another by the large region B and the region denoted as “Recording Zone Low Drive”. These are transition regions whose magnetic field strengths are not high enough to appreciably affect the media. Fig. 2.6 [14] shows two transitions (one north-north and one south-south) recorded at low frequency. The magnetized regions are bordered by transition zones (denoted by TZ) with ambiguous magnetizations. Fig. 2.7 shows higher frequency transitions.

In the hysteretic magnetization process discussed in Section 2.1.1, it was shown that the response of a magnet to an applied field was a function of the magnet’s previous magnetization state. This results in a highly nonlinear transfer curve, which is unacceptable for applications such as audio recording. To linearize the response of the magnet, analog audio recording signals are added to a high frequency sinusoid, on the order of 50-150 kHz. This technique is known as *AC bias*, and is similar in principle to the process of *anhysteretic magnetization*. In the description of hysteretic magnetization, it was shown that applying a strong cyclic field to a magnet with no net magnetization resulted in a transfer curve with no path returning to the unmagnetized state. However, if we gradually reduce the maximum amplitude of the applied field after each cycle, we can bring the magnetization back to zero [14]. Now, suppose we repeat this cyclic reduction process, but with a small constant field added to the larger cyclic field. The remanent magnetization left over after the cyclic field reduces to zero is proportional to the constant field. Fig. 2.8 [14] shows the transfer magnetization curve for anhysteretic magnetization, where the x -axis in this case represents

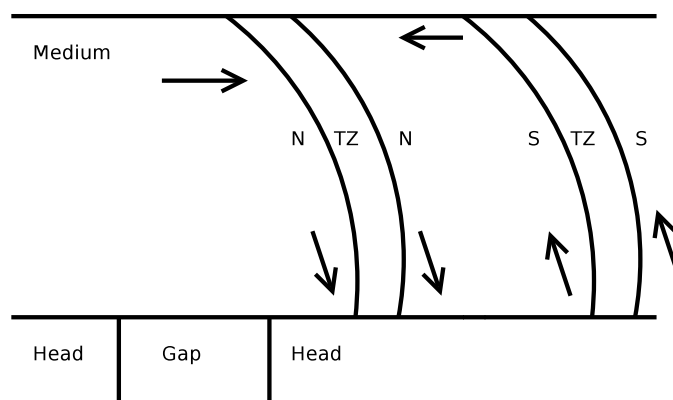


Figure 2.6: Write head near gap - two transitions. N denotes magnetic north and S denotes magnetic south. TZ denotes transition zone.

head electrically with an input signal, the stray magnetic fields from the magnetized media excite the head and induce the electrical signal. The reproduction process is somewhat simpler than the recording process in that it is linear, and so lends itself to analysis by superposition.

Consider the reproduction process shown in Fig. 2.9. The arrow points in the direction of motion of the tape. The magnetization of the media is simplified by assuming a series of bar magnets producing fringing lines of magnetic flux. Assuming an ideal ring head such as the one in Fig. 2.3 which collects all the available flux, the voltage induced in the head is given by [2]:

$$V = -N_{turns} \frac{d\phi}{dt} = -N_{turns} \nu_{tape} \frac{d\phi}{dx} \quad (2.6)$$

where ϕ denotes flux density, N_{turns} denotes the number of turns in the ring head coil, ν_{tape} denotes the tape speed, t denotes time, and x denotes displacement in the longitudinal direction. Considering a sinusoidal flux given by $\phi_{max} \cos(2\pi x/\lambda)$, the maximum voltage is [2]:

$$V_{max} = -\frac{2\pi N_{turns} \nu_{tape} \phi_{max}}{\lambda} = -2\pi N_{turns} \phi_{max} f \quad (2.7)$$

where E is the maximum voltage, ϕ_{max} is the maximum flux, and f is the frequency of the sinusoid induced in the reproduce head, in *hertz*. From these expressions, it can be seen

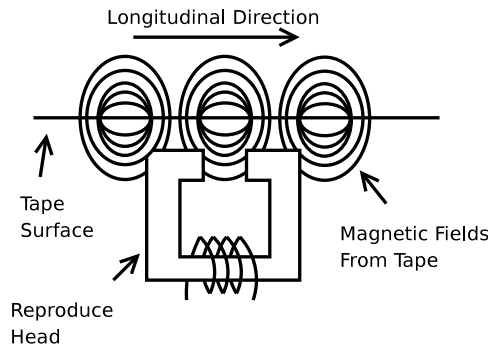


Figure 2.9: Ring head reproduction.

that the induced voltage is frequency dependent. If the induced voltage is used in this form, the reproduction is severely distorted, as higher frequencies induce higher voltage than lower frequencies. This effect is removed through a process known as *equalization*, which amplifies low frequencies relative to high.

2.3 Noise

This section presents an overview of the audio tape noise theory considered in the analysis of MFM data. The theory is primarily based on work performed by Mallinson [1] in considering noise as arising from two sources: the random distribution of magnetic particles in tape media and the random chance of magnetization of particles when exposed to an external magnetic field. The section then finishes with an overview of other theories pertaining to tape noise which suggest avenues for future analysis.

2.3.1 Noise Theory

Noise in particulate media can be considered as the result of two mechanisms: *writing noise* and *packing noise* [1]. The first arises as a result of randomness of magnetic moment orientation in unmagnetized media. The second is a result of the non-uniform distribution of magnetic particles in the media. In this section, we will examine these mechanisms and discuss their application to audio recording.

Writing noise occurs due to the statistical nature of the magnetization of particles. Unmagnetized media consists of particles whose dipole moments are randomly oriented such that the net magnetization of the media is zero. However, localized regions of the media may have some net magnetization, and this manifests itself in the reproduction process as noise. If a magnetizing field is applied, the particles have a chance of becoming magnetized as a result. The probability of this magnetization increases as a function of the applied field strength. This non-deterministic magnetization of individual particles is the core principal behind writing noise [1].

Consider a section of recording media with dimensions length L , width W , and thickness δy , as shown in Fig. 2.10 [1]. Assume that the medium has some average amount of magnetic

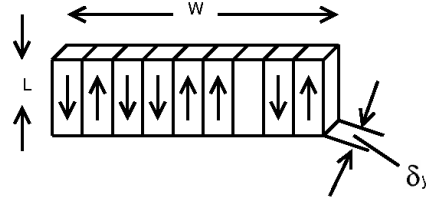


Figure 2.10: Row of magnetized particles. [1]

material per unit volume, denoted by \bar{P} . If the average volume of a single magnetic particle is \bar{v} , then the average number of particles in a section of media is given by [1]:

$$N = \frac{\bar{P}WL\delta y}{\bar{v}}. \quad (2.8)$$

Assume that the particles are identical, have the same physical orientation, and exhibit magnetization only in one of two directions (denoted by up and down), as in Fig. 2.10. Thus the particles can only assume one of two possible magnetization states. Further assume that each particle assumes the up state with probability p . Then, the magnetic dipole moment of this section of media can be written as [1]:

$$\mu_{total} = (+\mu_{particle})pN + (-\mu_{particle})(1-p)N = \mu_{particle}(2p-1)N \quad (2.9)$$

where $\mu_{particle}$ denotes the magnetic dipole moment of each particle. Normalizing this term by N yields [1]:

$$\bar{m} = \frac{\mu_{total}}{\mu_{particle}N} = (2p-1) \quad (2.10)$$

where the relationship between magnetization and p is evident. Assuming that N is large, the variance of $\vec{\mu}_{total}$ can be written as ¹ [1]:

$$\sigma^2 = \mu^2 N(1 - \bar{m}^2) \quad (2.11)$$

¹A full derivation of this result is given in Appendix I

Since the power of the noise is proportional to this variance, we can see that the writing noise power is maximized at a when the medium is unmagnetized, and is minimized when the medium is saturated [1]. This means that signals recorded with low write current amplitude will exhibit more noise than those written with high write current amplitude.

Packing noise arises due to the stochastic nature of the distribution of particles within a particular volume of the media. Suppose that all particles in the media are magnetized to saturation in the up direction. If the media is divided into equally spaced volumes, each individual volume will contain a different number of magnetic particles, which will be reflected in the amount of stray field generated by each of these volumes. This is the source of packing noise.

Consider the same scenario as in Fig. 2.10. Define the maximum number of particles capable of fitting into the volume of the row as [1]:

$$N_{max} = \frac{WL\delta y}{v} \quad (2.12)$$

where v denotes the volume of a particle. Also consider an experiment in which particles are distributed on the row in Fig. 2.10 according to a binomial distribution with $n = N_{max}$ and $p = \bar{P}$. It can be shown that the variance of the magnetic moment of the row is given by [1]:

$$\sigma_P^2 = (\bar{m}\mu)^2 N(1 - \bar{P}) \quad (2.13)$$

From this result it can be seen that the packing noise is highest at low values of \bar{P} and disappears when \bar{P} equals zero.

In media with relatively low packing densities, such as audio tape, writing noise and packing noise may be considered statistically independent of one another. So, the final expression for noise power becomes [1]:

$$\sigma_{total}^2 = \sigma_{writing}^2 + \sigma_{packing}^2 = \mu_{particle}^2 N(1 - \bar{m}^2 \bar{P}) \quad (2.14)$$

In AC biased recording, maximum signal levels are approximately $20 - 30\bar{P}$ for a typical audio tape being 0.4, the range for maximum noise power becomes $0.984 \bar{N}$ and $0.964 \bar{N}$ [1].

From this it can be seen that noise power varies very little over with respect to magnetization, suggesting that noise power can be considered constant in audio tapes.

2.3.2 Noise Overview

In this section, we survey several pieces of literature regarding noise in magnetic recording media. The previous section introduced a particular model of media noise which is tested in Section 4.1.3 using experimental MFM data. Suggestions for bringing the model predictions into better agreement with experiment included refining data collection techniques and re-evaluating the model itself. The goal of this section is to facilitate further refinement to the model by discussing literature related to media noise.

Silva and Bertram [15] studied magnetization fluctuations in uniformly magnetized thin-film recording media. The noise was quantified by power spectral density, which was found to fit a Lorentzian pulse shape. From experimental measurements it was determined that noise power is concentrated in the center of magnetic transitions, which was also suggested in the model in Section 2.3.1. At magnetization states far from zero, the data suggested that the noise process was driven by medium inhomogeneities, such as surface roughness. It was shown that this noise is proportional to the squared derivative of the hysteretic remanance loop, $(d\vec{M}/d\vec{H})^2$, where \vec{M} is the sample magnetization and \vec{H} is the field applied to the sample [16]. This factor was not taken into account in the model we considered.

The physical properties of the magnetic particles themselves were considered Denteneer and Cramer [17] and Luo and Bertram [18]. Common assumptions about particle size were presented, including independently distributed particle length, radius, and magnetic moment direction. It was shown that introducing a correlation between particle volume and length improves noise predictions yielded by several media models. Also shown is that noise spectra is generally dependent on the wavelength of the recorded sinusoid. A similar relationship was shown by Giljer et. al. [19], where recording density was found to be inversely proportional to signal-to-noise ratio. In Luo and Bertram [18] showed that assuming statistically independent spacing for particles leads to inaccurate noise predictions. Realistic physical effects such as particle clustering and chaining were considered. Further spatial distributions for noise were

discussed by Alex et. al. [20].

Yuan and Bertram [21] and Roesler et. al. [22] use a technique known as the Karhunen-Loève (K-L) expansion to characterize media noise. This technique empirically re-expresses noise data as an orthonormal expansion of orthogonal eigenfunctions. Dominant noise features can be inferred from the data in this way. Yuan and Bertram [21] identified noises induced by transition center shifting (jitter), transition width fluctuation, amplitude modulation, and combined effects by the most principal eigenfunctions. This makes the K-L expansion useful for identifying dominant noise sources from several different physical phenomena. The K-L expansion was applied to experimental data and it was determined that 80% of noise power is caused by jitter, amplitude modulation, and pulse width modulation of the recorded pulse waveforms.

This section presented several potential physical mechanisms of magnetic media noise and methods for quantifying that noise. Physical factors include medium inhomogeneity, variations in the squared derivative of the remanence loop, physical orientation, spacing, and dimensions of magnetic particles, particle clustering and chaining and others all contribute to noise power. Noise quantification techniques such as power spectral density and Karhunen-Loève expansions were discussed. All of these factors provide motivation for improvements to the model in Section 2.3.1.

Chapter 3

Magnetic Force Microscopy Principles of Operation

Chapter 3 presents an introduction to the microscopy technique known as *magnetic force microscopy* (MFM). MFM provides high resolution imaging of magnetic fields emanating from a sample. The overview section first presents a general overview of scanning probe microscopy (SPM), the technique from which MFM is derived. A block diagram of the magnetic force microscope is then presented, followed by a simple model of the interaction of the microscope with the sample.

The last section considers modeling in more detail. A Fourier-domain approach to recovering the magnetization distribution of a sample using MFM is presented. The results of simulation of MFM are given and compared with actual data collected using the instrument.

3.1 An Overview of MFM

This section presents a block diagram of magnetic force microscopy and its fundamental operating principles. A model of the MFM is given as is a description of a simple one-dimensional simulation of the MFM's response to longitudinal recording media.

3.1.1 Scanning Probe Microscopy

Scanning probe microscopy (SPM) is a technique for collecting data from the surface of materials at very high resolutions, typically on the order of nanometers. This high resolution is achieved by measuring interaction forces between a very small probe and the sample surface. The probe consists of a sharp tip (radius of curvature: $3 - 50 \text{ nm}$ [23]) at the end of a flexible cantilever, which is flown over the sample surface and interacts with it in a fashion determined by the mode of operation. SPM is not limited in resolution by diffraction, as is optical microscopy, nor does SPM require extensive sample preparation, as does electron microscopy. An example application of SPM is observing the effect of medications on AIDS viruses by imaging the viruses themselves [24].

There are many different modes of SPM. The most common are *atomic force microscopy* (AFM) and *scanning tunneling microscopy* (STM). AFM measures the physical interactions between the tip and the sample. For example, the tip can literally be dragged across the surface, and the force of interaction measured. STM measures the electric current flowing between the sample and the electrified probe. Magnetic force microscopy, which is similar in operation to AFM, is the technique we are concerned with in this research. MFM measures the magnetic interactions between the magnetized tip and sample.

3.1.2 MFM Subsystems

A magnetic force microscope is composed of several subsystems, as shown in Fig. 3.1(a) [25]. The most critical component of the microscope is the magnetic tip, which is the sensing portion of the microscope [26]. If the tip is attached to the end of a flexible cantilever, oscillated, and flown over the sample, its magnetic properties cause it to interact with the stray magnetic fields from the sample. The phase of the tip is measured by a non-perturbing detection scheme, such as the diode laser and photo diode shown in the block diagram. The position of the tip is controlled by the scanner, the most common being a piezo-electric tube scanner which moves the sample under the tip [25]. The controller sends movement instructions to the scanner. A computer collects data from the photo diode and sends instructions to the controller.

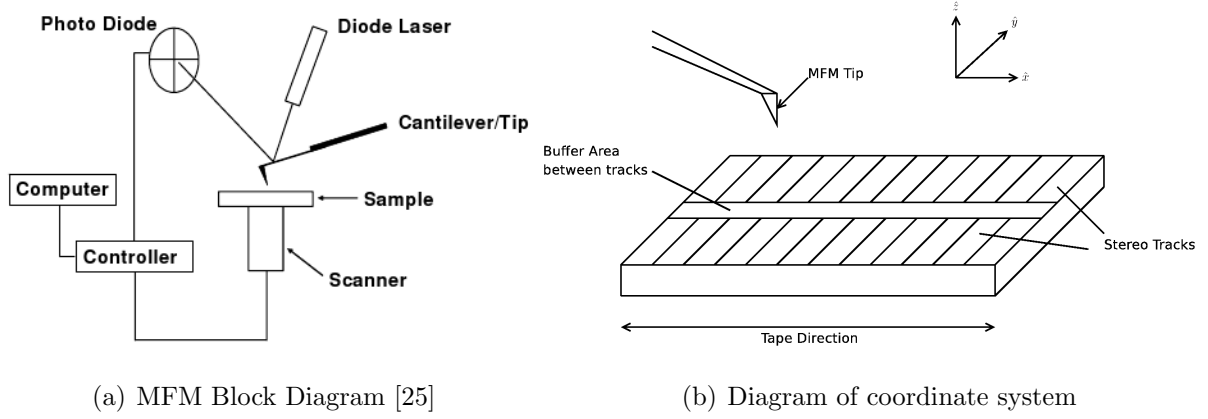


Figure 3.1: (a) Block diagram of magnetic force microscope and (b) diagram of coordinate system in the vicinity of the MFM tip.

The fundamental operating principle of the MFM is the detection of a gradient magnetic force by a resonance frequency shift of the oscillating cantilever. The cantilever is driven at its resonance frequency, ω_0 . If an external magnetic force is present in the vicinity of the tip of the cantilever, it exerts a force on the magnetic tip. It will be shown that the derivative of this force is proportional to the output of the microscope. The net effect of this force is to modify the spring constant of the cantilever and shift its resonant frequency[6]. This shift manifests as a phase shift between the cantilever's driving oscillator and the oscillation of the cantilever itself. Since the magnetic force felt by the tip from the sample is not constant in space, it is referred to as a *magnetic force gradient* or simply *force gradient*:

$$F'_{tip} = \frac{dF_{tip}}{dz}. \quad (3.1)$$

From this point on, without further qualification, it should be assumed that F'_{tip} is taken in the z direction, and that the tip oscillates only in the direction of the z -axis. The tip's actual path of deflection is of course more complicated than this, but for the purposes of illustrating the resonance frequency shift, this assumption is helpful. If a force gradient is present in the vicinity of the oscillating tip, the resonance frequency will be approximately reduced by [6]:

$$\Delta\omega = \frac{\omega_0 F'_{tip}}{2k} \quad (3.2)$$

where k is the cantilever spring constant. A shift in the resonant frequency of the cantilever will cause a corresponding shift in oscillation phase, given approximately by [27]:

$$\Delta\phi = \frac{Q}{k} F'_{tip} \quad (3.3)$$

where $\Delta\phi$ represents the shift in oscillation phase and Q is the quality factor¹ of the resonance. Of course, $\Delta\phi$ varies as the tip moves over the sample. This phase shift is taken as the output of the microscope.

3.1.3 A Mathematical Model of MFM

To better understand the relationship between medium magnetization and microscope output, a model of the interactions between magnetic tip and medium is presented. An ideal point dipole is used to model the tip, along with a two-dimensional model of longitudinal recording media. These are combined to produce a simulation of the MFM response.

The force on the magnetic tip results from the interaction energy between the tip and the sample, as given by the following relation [29]:

$$F_{tip} = \nabla E_{tip-sample} \quad (3.5)$$

where F_{tip} denotes the force on the tip and $E_{tip-sample}$ is the interaction energy between the tip and sample. The interaction energy in the most general case is given by [29]:

¹The quality factor of an oscillating system is a measure of the sharpness of the resonance curve of the system. The resonance curve is a graph of oscillation amplitude versus driving frequency. A higher quality factor indicates that the oscillation amplitude of the system drops off very quickly as the driving frequency diverges from the system's natural frequency. The expression for the quality factor is [28]:

$$Q = \frac{\omega_d}{2\gamma} \quad (3.4)$$

where Q is the quality factor, ω_d is the frequency of the oscillator while freely running, and 2γ is the frequency range bounded by the points on the resonance curve at which oscillation amplitude has dropped by a factor of $1/\sqrt{2}$ of the maximum amplitude.

$$E_{tip-sample} = \iiint_{G_{tip}} \vec{M}_{tip} \cdot \vec{H}_{sample} dx dy dz \quad (3.6)$$

where \vec{M}_{tip} is the magnetization of the tip and \vec{H}_{sample} is the stray field from the sample. Of course, both \vec{M}_{tip} and \vec{H}_{sample} are functions of x, y , and z . The term G_{tip} on the integral denotes that this is a volume integral over the entire volume of the magnetic tip. Since measuring the exact magnetization of the tip itself is difficult, an approximation is typically made that considers the tip as a point magnetic dipole. Using this assumption and combining (3.5) with (3.6) [29]:

$$F_{tip} = (\vec{m} \cdot \nabla) \vec{H}_{sample} \quad (3.7)$$

where $\vec{m} = \vec{M}_{eff} G_{eff}$, \vec{M}_{eff} is the effective dipole moment and G_{eff} is the effective volume of the tip. G_{eff} varies from G_{tip} above in that G_{eff} denotes the total volume of the tip, while G_{tip} denotes the limits of integration corresponding to the tip dimensions in (3.6). A further assumption is made that tip-sample interaction is primarily in the z -direction [29]. This causes (3.7) to take the form:

$$F_{tip} = m_x \frac{\partial H_x}{\partial z} + m_y \frac{\partial H_y}{\partial z} + m_z \frac{\partial H_z}{\partial z} \quad (3.8)$$

where m_x , m_y , and m_z are the spatial components of m and H_x, H_y , and H_z are the spatial components of \vec{H}_{sample} . As discussed in the previous section, the output from MFM is proportional to the derivative of the force on the tip. Differentiating (3.8),

$$F'_{tip} = m_x \frac{\partial^2 H_x}{\partial z^2} + m_y \frac{\partial^2 H_y}{\partial z^2} + m_z \frac{\partial^2 H_z}{\partial z^2} \quad (3.9)$$

After establishing the tip model, an appropriate model for the stray fields from the recording media must be presented. Since the MFM tip senses fields primarily in the z direction, and our model assumes a tip only sensitive to fields in that direction, the x and

y components of field are excluded in the medium model. The z component of the field reaches a maximum magnitude at a north-to-north or south-to-south magnetic transition. A common model in recording physics of the magnetic transition is the Williams-Comstock model, which leads to a field expression for a single bar magnet of the form [6]:

$$H_z(x, z) = 2M_r \log \left(\frac{x^2 + (\delta + z + a)^2}{x^2 + (z + a)^2} \right) \quad (3.10)$$

where M_r is the remanent magnetization of the medium, a is the transition width, δ is the media thickness, x is the displacement in the longitudinal direction, and z is the displacement in the direction normal to the sample. Here, the transition is assumed to be infinitely long in the cross-track direction. The transition width parameter is calculated from [30]:

$$a = 2\delta M_r (3.3 - 2.3S^*) / H_c \quad (3.11)$$

where H_c is the coercivity, and S^* is the *coercivity squareness*, which describes the possible deviation in the media coercivity. A series of transitions (magnets) is modeled as a superposition of individual transitions [6]:

$$H_{total}(x, z) = \sum_n (-1)^n H_z(x - nd, z) \quad (3.12)$$

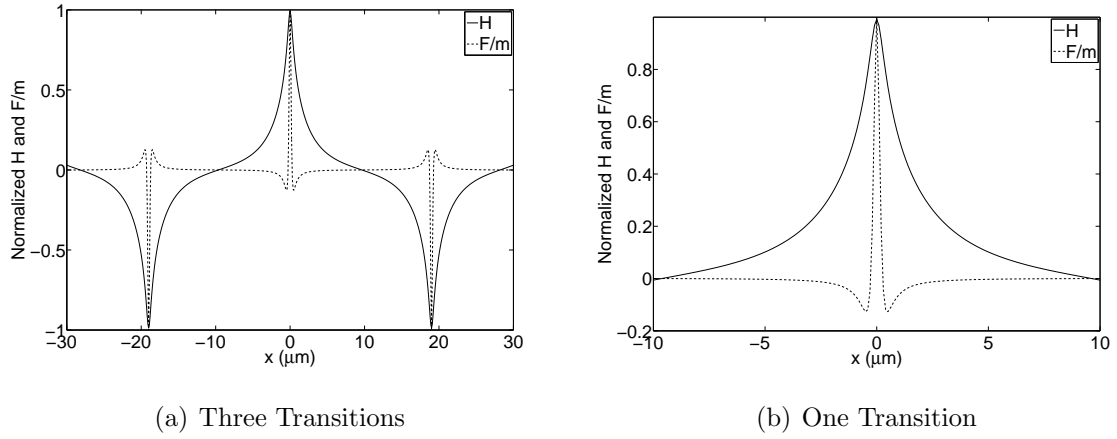
where n is an integer and d is the distance between transitions.

It is now possible to simulate the output of the MFM for a typical measurement scenario. The simulation parameters are taken from the properties of common analog audio tapes, and are summarized below.

Fig. 3.2(a) shows three simulated magnetic transitions and the MFM response. The positive peaks correspond to north-to-north transitions, and the negative peaks correspond to south-to-south transitions. Fig. 3.2(b) shows a single magnetic transition in finer detail. These modeling results will be useful in Section 3.2 when comparing actual MFM data to theoretical results.

Parameter	Symbol	Value
Material	N/A	$\gamma - Fe_2O_3 + Co$
Remanent Magnetization	M_r	140 kA/m
Magnetic Layer Thickness	δ	$5 \text{ }\mu\text{m}$
Distance Between Transitions	d	$19 \text{ }\mu\text{m}$
Tip Scanning Height	z	200 nm
Transition Width	a	$0.51 \text{ }\mu\text{m}$
Coercivity	H_c	52 kA/m
Coercivity Squareness	S^*	0.598

Table 3.1: Parameters for MFM response simulation.

Figure 3.2: Simulated MFM response to audio recording media showing magnetic transitions. Normalization constants are $723 \text{ Oe}(H)$ and $3.28 \times 10^{15} \text{ N}/\mu\text{m}(F/m)$.

3.2 Magnetization Estimation using MFM Images

This section outlines the procedure for recovering the magnetization patterns of the tape sample using MFM data. The MFM is treated as a linear space-invariant system, which is completely described by its response to a “point” magnetic charge. The MFM’s response is simulated, and the results of simulation are given in Section 3.2.2.

3.2.1 Magnetization Estimation through Tip Response Function

Magnetic force microscope images yield information about the stray magnetic fields emitted by a sample. However, as was shown Section 3.1.3, the data given by the MFM depends not only on the stray fields themselves, but also the magnetic properties of the tip. Imaging

the same sample using different tips will yield different results. To remove the information about the tip, a recovery technique is needed which takes into account the specific magnetic properties of the particular tip being used. When the coercivity of the tip is more than the magnetic field strength of the stray sample fields, and the coercivity of the medium is more than the strength of the fields emitted by the tip, the MFM can be classified as a *linear space-invariant* system (LSI) [31]. In other words, the properties of the MFM tip do not change as the tip moves over the sample. This makes the analysis of MFM data amenable to Fourier techniques. In this section, a method for obtaining the *impulse response function* of the MFM tip under the LSI condition is discussed, and simulations are used to show the results of using this function for obtaining magnetization estimates.

A system which is linear and invariant in the independent variable over which it is measured can be completely characterized by its impulse response. In many cases the independent variable is time, but in the case of the magnetic force microscope, the independent variable is space, which denotes the position of the MFM tip relative to the sample. The input-output relationship for a general two-dimensional LSI system in the spatial domain is given by:

$$y(s_1, s_2) = \iint x(s_1, s_2) h(s_1 - s'_1, s_2 - s'_2) ds'_1 ds'_2 \quad (3.13)$$

where y is the output, x is the input, h is the impulse response function, s_1 and s_2 are coordinates denoting the position in space to be evaluated, and s'_1 and s'_2 are variables of integration which range over the entire space under analysis.

The crucial component in the input-output relationship is $h(s_1, s_2)$, the impulse response function, or simply *impulse response*. Finding this function for the MFM involves determining the microscope's response to an isolated "point" magnetic charge. When referring specifically to the impulse response of the MFM, the term *dipole response function* or *dipole response* is used. Strictly speaking, a point magnetic charge is not physically realizable. However, a reasonable approximation can be obtained by imaging the end of a nanoscale single-domain nickel strip [10]. Typical lengths for these strips are on the order of 70 nm. A simulated dipole response function is shown in Fig. 3.3. Once the dipole response is known,

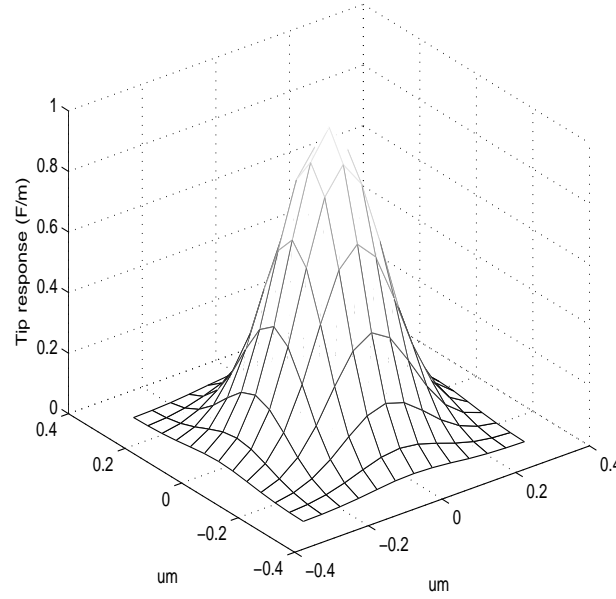


Figure 3.3: Simulated dipole response function.

the input-output relationship of the MFM becomes [10]:

$$G(x, y) = \iint M(x', y') D(x - x', y - y') dx' dy' \quad (3.14)$$

where $G(x, y)$ is the MFM image, M is a quantity representing the magnetic charge distribution of the media, D is the dipole response function, x and z are the coordinates denoting the position of the MFM tip over the sample, and x' and y' are variables of integration. A comment must be made on the nature of $M(x, y)$ and $D(x, y)$. In general, the magnetization of the media is a function of three spatial variables, and can be considered as yielding a scalar value at each point representing the magnetic charge distribution. However, the MFM is only capable of recovering information about the magnetization in the plane of the media, and gives no information about the distribution of magnetization depth-wise (along the z -axis) within the media [32]. The MFM essentially sees the sample magnetization as a flat, two-dimensional distribution of magnetic charges. For this reason, $M(x, y)$ becomes a two-dimensional function of two variables, as does $D(x, y)$. Furthermore, the MFM alone

cannot given any information about the solenoidal ² component of magnetization, since this component is not field producing [33].

Equation (3.14) can be represented in the Fourier domain by:

$$G(x, y) = \mathcal{F}^{-1}[\mathbf{M}(k_x, k_y)\mathbf{D}(k_x, k_y)] \quad (3.15)$$

where k_x and k_y are the spatial frequency variables in the in-track and cross-track directions, $\mathbf{M}(k_x, k_y)$ is the Fourier Transform of the magnetization distribution components $M(x, y)$, $\mathbf{D}(k_x, k_y)$ is the Fourier transforms of the dipole response distribution components $D(x, y)$, and the operator \mathcal{F}^{-1} denotes the inverse Fourier transform. (3.14) represents the output of the MFM as a function of the magnetization distribution of the sample. This expression can be rearranged to yield the magnetization distribution as a function of MFM output [10]:

$$M(x, y) = \mathcal{F}^{-1} \left[\frac{\mathbf{G}(k_x, k_y)}{\mathbf{D}^*(k_x, k_y)} \right] \quad (3.16)$$

where \hat{x} and \hat{y} are the in-track and cross-track directions, and $\mathbf{G}(x, y)$ is the Fourier Transform of the MFM image, $G(x, y)$, and the asterisk in $\mathbf{D}^*(k_x, k_y)$ denotes complex conjugation. This expression shows the transformation from an MFM image $\phi(x, y)$ into a magnetization distribution $M(x, y)$. The next section discusses implementing these algorithms numerically and applying them to MFM image simulation.

3.2.2 Simulated MFM Images

In the previous section, a method for characterizing MFM as a linear space-invariant system was presented. It was shown that MFM is completely characterized by a two-dimensional impulse response function. Given this function, an MFM image can be generated using simulated magnetization patterns, and the magnetization patterns themselves can be recovered from images. However, all of the analysis was presented in continuous space. To implement these algorithms numerically, two-dimensional Fast Fourier Transforms are utilized. In this section, several images are presented to demonstrate the procedure. Example code which

²A solenoidal vector field is a vector field with divergence zero.

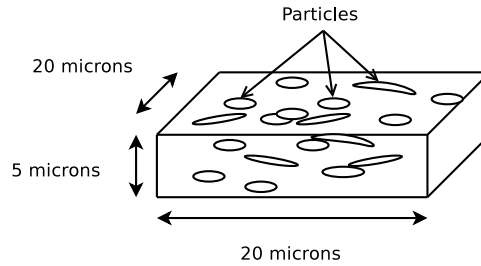


Figure 3.4: Particle model used to generate magnetization patterns.

illustrates this process is available from the WVU ETD site where this thesis was obtained, in the file “codelisting.pdf”.

To simulate the response of the MFM, simulated magnetization patterns are generated. These patterns represent common recording conditions in analog audio tape. As discussed in Subsection 2.3.1, audio tapes consist of randomly oriented magnetized particles deposited in a nonmagnetic substrate. A section of randomly magnetized particles is simulated under the following conditions. The particles are assumed to be pairs of magnetic point monopoles with spacing $1\ \mu\text{m}$ embedded in a three dimensional lattice of width and length $20\ \mu\text{m}$, and depth $5\ \mu\text{m}$. The particle locations are generated by first placing the particles at points $1.5\ \mu\text{m}$ apart in the x , y , and z directions, and then adding a Gaussian random variable to each of these dimensions for each particle. This results in an average particle density of about $4\ \text{particles}/\mu\text{m}^3$, and is illustrated in Fig. 3.4. This particle density is considerably less than average particle densities for audio tape given in Table 2.1, resulting in a less precise model but faster simulation. However, as will be shown in the simulated MFM image, the overall magnetic field structure is still comparable and serves the purpose of demonstrating the analysis techniques presented above.

Equations (3.14) and (3.16) are implemented numerically, in modified vector form, by two-dimensional Fast Fourier Transforms (FFTs). Since magnetic charge distribution is a scalar quantity, and magnetization is a vector quantity, this modification into vector form is necessary. However, both forms yield a scalar MFM image so that the distinction is not major in this case. The tip response function is applied in the form of Equation 3.16 to actual data, not in vector form. Example code which illustrates the application of the tip response

function to data is available from the WVU ETD site where this thesis was obtained, in the file “codelisting.pdf”. The MFM images are windowed by a Kaiser-Bessel window with parameter $\alpha = 2$ such that they fall to 0 at their edges. This is done to minimize spectral leakage in the resulting FFTs. The tip response function used in the simulation is described by a two-dimensional Gaussian function:

$$D(x, z) = Ae^{-([\frac{x}{\sigma_x}]^2 + [\frac{z}{\sigma_z}]^2)} \quad (3.17)$$

with $A = 1$ and $\sigma_x = \sigma_z = \frac{1}{\sqrt{40}}$. It should be noted that since the FFT is applied to data with finite length, there will be a lower limit on the frequencies which can be represented, which is a function of MFM image size. For an MFM image $90 \times 90 \mu m$ in size, the lower frequency limit is:

$$f_{low} = \frac{\nu_{tape}}{w_t} \quad (3.18)$$

where ν_{tape} is the tape speed and w_t is the width of the image in the longitudinal direction. For typical values of tape speed and image width, f_{low} is on the order of 500 Hz .

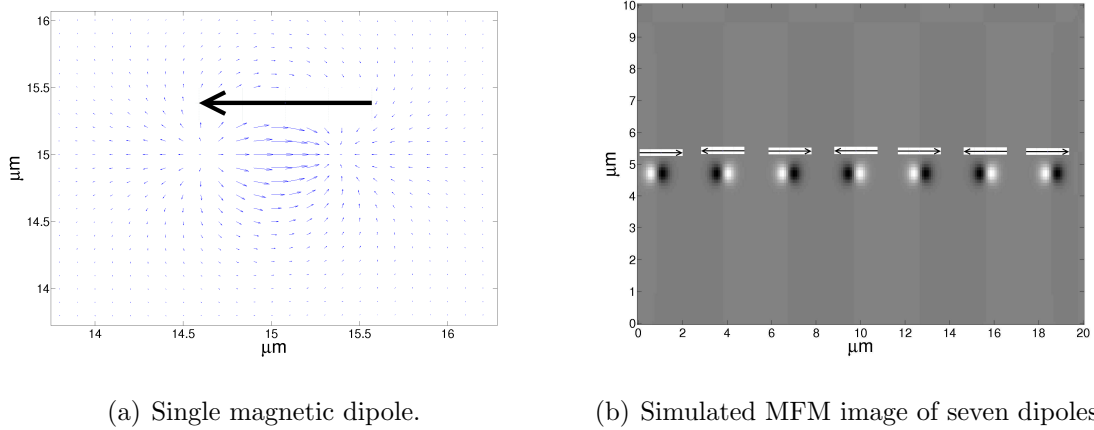


Figure 3.5: Single magnetic dipole (a) shown with a simulated MFM image of seven dipoles (b).

The field lines for a single magnetic dipole are shown in Fig. 3.5(a). The large black arrow denotes the south-to-north transition. Several of these dipoles having different rotations and

offsets within the media are summed to form the simulated media magnetization. Some comments must be made about the general characteristics of this dipole. The arrows in the image represent point magnetic moments. The regions of radially pointing areas represent the center points of the magnetic monopoles. Points with arrows converging on them represent magnetic south poles, while points with arrows diverging from them represent magnetic north. A simulated MFM image of seven of these magnetic dipoles oriented head-to-head and tail-to-tail is shown in Fig. 3.5(b). Again, the black arrows denote the south-to-north transition.

A pair of field maps is shown in Fig. 3.6. The first image, Fig. 3.6(a), is the original field map generated by simulation. Fig. 3.6(b) is the field map recovered by the relationship given in (3.16). Clearly, the recovered map closely resembles the original field map. However, because a windowing function is applied to the data prior to computing the two-dimensional FFT, the magnitudes of the vectors in the recovered image fall to zero near the edge of the image. While this windowing process removes edge data, it reduces spectral leakage, and improves the fidelity of the remaining data.

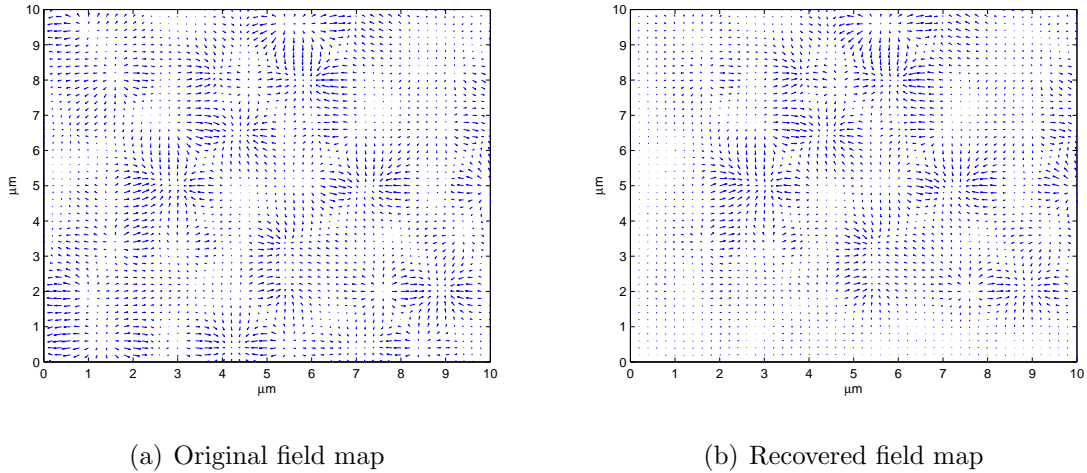


Figure 3.6: Simulated magnetization map of a cross-section of the particle model. Image (a) is the original and image (b) is the recovered image.

The simulated MFM image is shown in Fig. 3.7 next to an actual MFM image. As noted above, the particle densities used in the simulation are smaller than those in actual audio tape, resulting in more roughness as compared to the actual MFM image. However, the

images possess similar characteristics, such as obvious north-to-south magnetic transitions (areas of transition from black to white) and random transition orientations. This is a useful proof of concept for the recovery techniques in Chapter 4.

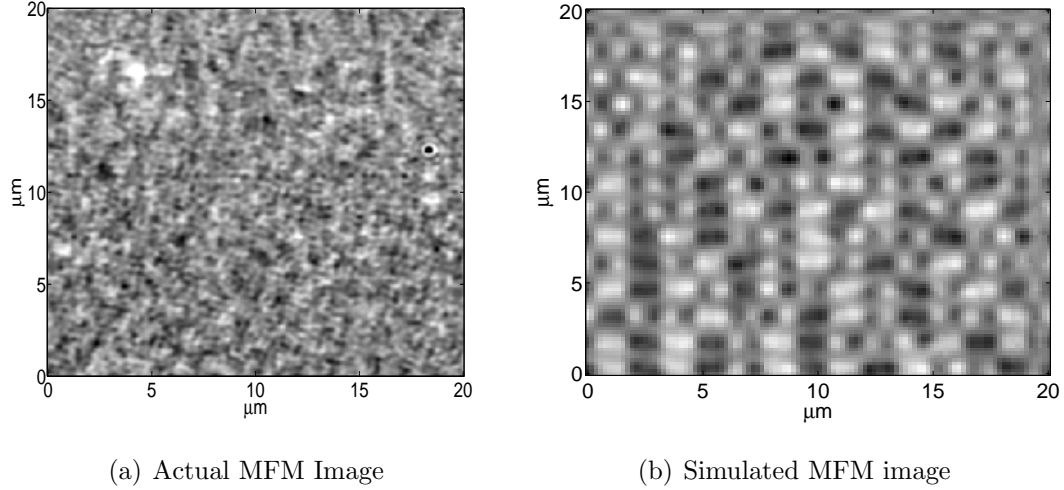
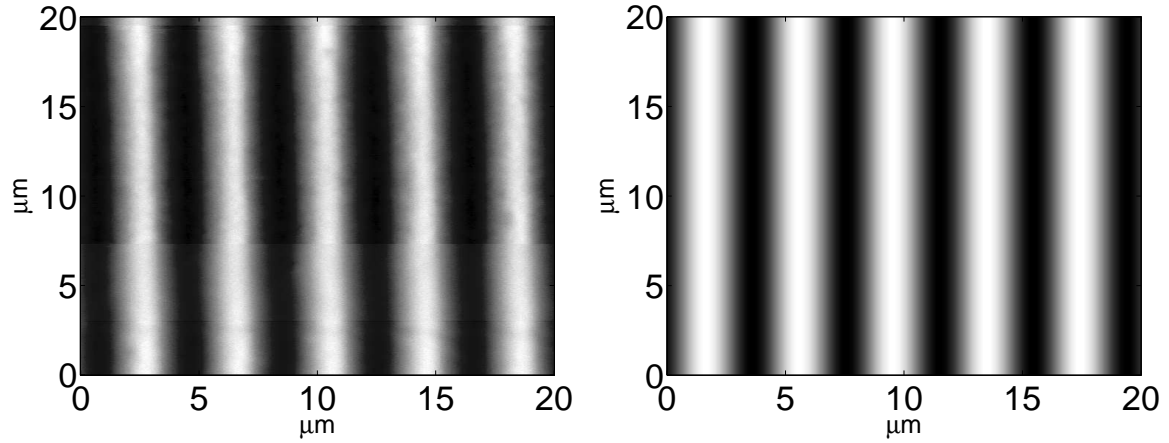


Figure 3.7: MFM image of a noisy audio recording vs a simulated MFM image of a noisy magnetic field map.

3.2.3 Data Comparison

The previous section presented several simulated MFM images and field maps. This data was shown to illustrate the recovery of magnetization patterns from MFM images. However, the magnetization patterns were chosen to be random. In this section, several more simulated MFM images and field maps are shown, this time with basic structure. The magnetization patterns are chosen to simulate a recording of a sinusoidal signal.

Figure 3.8(a) shows an MFM image of a sinusoid recorded on a standard analog audio tape. The dark and light areas vary sinusoidally over a grayscale intensity level across the image width, and represent the magnitude of the magnetization. The noise in the image is approximately white, while the image beside it, Figure 3.8(b) appears noiseless. This is because the noiseless image is an ideal simulation of a sinusoidal magnetization pattern. However, even in the absence of noise, a resemblance is apparent between the images. A similar situation is shown in Figure 3.9. Instead of only a single sinusoid, the recording

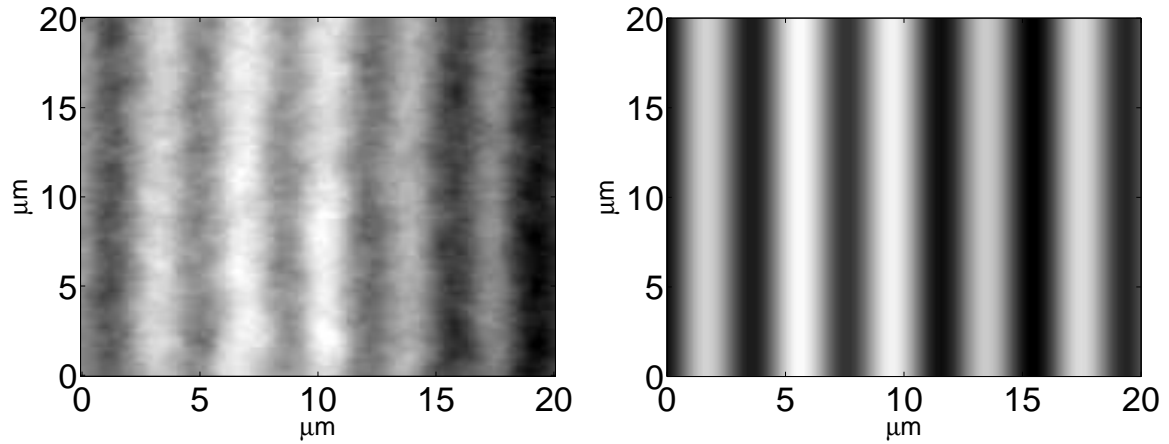


(a) Sample MFM image showing a recorded sinusoid, $f = 12 \text{ kHz}$

(b) Simulated MFM image of a sinusoidal magnetization pattern, $f = 12 \text{ kHz}$

Figure 3.8: Comparison of MFM images to simulation - single tone.

is a sum of two sinusoids at different frequencies. Generating and analyzing these simple magnetization patterns will provide the basis for data analysis in Chapter 4.



(a) Sample MFM image showing a recorded sum of sinusoids, $f_1 = 1.5 \text{ kHz}$, $f_2 = 12 \text{ kHz}$

(b) Simulated MFM image of a sinusoidal magnetization pattern at two different frequencies $f_1 = 4.8 \text{ kHz}$, $f_2 = 12 \text{ kHz}$

Figure 3.9: Comparison of MFM images to simulation - multiple tones.

Chapter 4

Analysis of Noise and Erasure

In this chapter, analysis of signal erasure, media noise, and overwrite are investigated using several MFM images. First, physical mechanisms of tape erasure are presented, such as bulk and head erasure. A discussion of the frequency dependency of erasure is given. Next, the phenomenon of partial erasure, defined as arising when magnetic fields interact destructively, is discussed. Then, an analysis of noise is given and comparison with the theoretical model given in Subsection 2.3.1 is presented. Finally, an analysis of signal recovery after erasure is presented. Single tone data, multi-tone data, and *in situ* erased data are investigated. Fast Fourier transforms and estimated SNR's (signal to noise ratios) are given, along with a discussion of the feasibility of signal recovery by this method.

4.1 Erasability and Overwrite of Media

This section first discusses the different methods of erasure, such as bulk erasure and head erasure, and their relative merits. The re-recording phenomenon is discussed as a motivation for attempting to recover erased signals. Efficiency of erasure techniques is discussed and quantified. Evidence is presented to suggest that the erasure process is frequency dependent. The phenomenon of partial erasure is discussed, in which magnetic fields destructively interfere with each other and lower the measured SNR. A processing technique is presented which attempts to remove the effects of partial erasure. Finally, the noise theory discussed in previous sections is compared with experimental data by computing the variance of the

magnetic dipole moment measured in the images.

4.1.1 Erasure Techniques and Overwrite

This section investigates the erasability of audio tape recordings and criteria which can be used to quantify erasure. Erasure techniques used in audio tape can be divided into bulk erasure and head erasure. Bulk erasure involves applying a strong alternating, decreasing magnetic field to the entire medium at the same time. The initial amplitudes for this field are typically at least five times the coercivity of the medium [2]. This technique yields a more complete erasure than the alternative, erasure by head. In audio tape recording, erasure through the use of a head is far more common.

As discussed in Subsection 2.1.2, there are two types of erase heads, permanent magnet (DC) erase heads, and inductive heads which are excited by AC current, producing alternating magnetic fields. While AC erase heads typically produce a better erasure than DC, they also give rise to a potential “re-recording” effect, in which the section of the media under erasure is re-recorded by the stray fields from the adjacent media which have not been erased. In this case the AC erase field acts as a bias field, which was discussed in Subsection 2.2.1. Efficient head design can minimize this effect [34]. Efficiency of erasure is defined by the *erase ratio*, which is defined as the ratio of the signal energy before and after erasure [34]:

$$R_e = 20 \log \left(\frac{E_{ae}}{E_{be}} \right) \quad (4.1)$$

where R_e is the erase ratio in dB , E_{ae} is the remaining signal energy after erasure, and E_{be} is the signal energy before erasure. The goal of a well-designed erase head is to achieve an erase ratio greater than $-70dB$ [34].

As studied in [35], longer wavelength signals tend to record more deeply than shorter wavelength signals, providing evidence that shorter wavelength signals may be detectable after overwrite. As a measure of MFM’s ability to recover erased data, the FFT is used to compute energy after erasure of a written sinusoid, and compared with the FFT magnitude of the sinusoid prior to erasure. The signal-to-noise ratio (SNR) is then computed, which

is essentially the inverse of the erase ratio as defined above. Another analysis which will be presented is modeled after the experiment performed in [36], in which erasure is performed by an electromagnet placed directly under the MFM sample *in situ* in the microscope. This will allow a specific area of tape to be measured several times in different magnetization states. The results of these analyses are presented in the next chapter.

4.1.2 Partial Erasure

This section considers the magnetic phenomenon known as *partial erasure*. Partial erasure is defined as the erasure that occurs when physically adjacent magnetic grains (or their stray fields) in recording media interact destructively, forcing the magnetization in that area below some threshold [11]. Yen et. al. [37] suggest that above a certain critical density of magnetic flux transitions in magnetic media, the transitions effectively annihilate each other, which has implications for the interpretation of signals erased by a high frequency AC bias. Partial erasure can be further subdivided into *linear* and *nonlinear* partial erasure. Linear partial erasure is defined as the destructive interaction of stray fields from adjacent magnetic grains. Nonlinear partial erasure however occurs when the magnetic grains themselves interact and change their magnetization states. Taguchi et. al. [11] investigate the phenomenon in a digital recording system with high density of magnetic material. Since our recording media is analog audio tape, which is relatively low density, we will restrict our investigation to linear partial erasure, ignoring inter-particle interactions.

To confirm or deny the presence of partial erasure in our data, the following experiment is performed:

1. A set of MFM images is chosen for investigation. The set consists of three images: one showing a strong signal, one showing an erased signal, and one showing a partially erased signal. These were chosen to observe the effect of signal strength on partial erasure.
2. For each image in the set, partial erasure is computed using the following criterion used by Taguchi et. al. [11]:

- Compute the arithmetic mean for the field strength in each column of the MFM image, where each column runs across the track.
- Compute a threshold using the following formula:

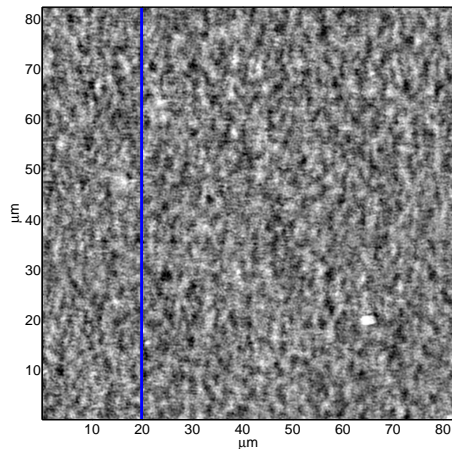
$$T = 0.3|m| \quad (4.2)$$

where m is the arithmetic mean for a particular column and T is the threshold.

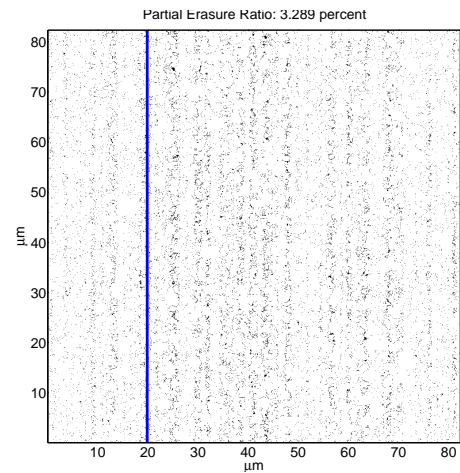
- For each pixel in the column, compare the pixel's magnitude with the threshold. If the pixel magnitude is less than the threshold, consider that pixel an area of partial erasure.
3. The above procedure will result in a boolean image where black values represent partial erasure and white values represent no partial erasure. At the top of each image, a percentage value representing the percentage of the image flagged as partial erasure is given.
 4. A line profile of the column having the highest amount of partial erasure is plotted.
 5. To investigate the effect of partial erasure on the spectrum of the data, the pixels marked as partial erasures are replaced by the arithmetic mean of the pixels surrounding them. The FFT is then computed for this new MFM image.

Once the experiment is performed, a discussion is presented regarding how the results affect potential data recovery.

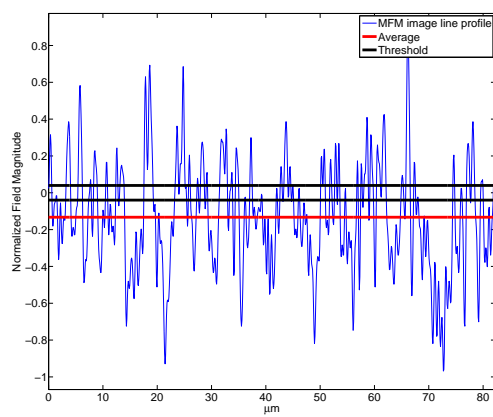
The three figures, Fig. 4.1, Fig. 4.2, and Fig. 4.3, show the partial erasure data for the erased signal, partially erased signal, and strong signal respectively. An immediately interesting result is that the partial erasure ratio is highest in the image in which the signal has been partially erased, taking a value of 7.79%. In the erased image and partially erased images, partial erasure appears to be roughly uniformly distributed. However, as the signal strength increases, it appears that regions of partial erasure begin to exhibit a certain periodicity related to the regions of smallest field magnitude (gray regions in the MFM images). While these results are not absolutely conclusive evidence of the presence of partial



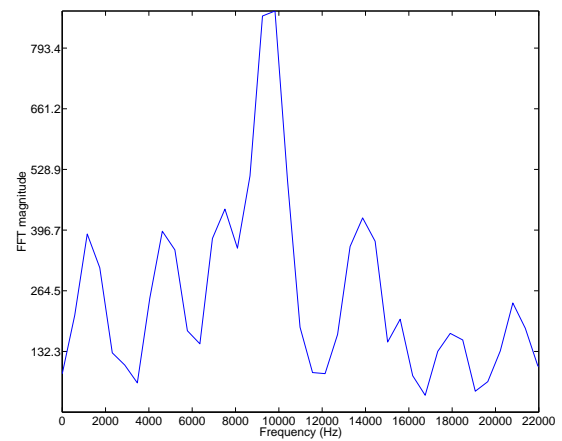
(a) MFM image - erased area



(b) Potential areas of partial erasure

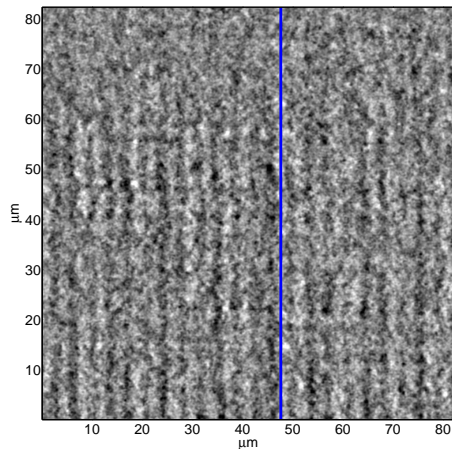


(c) Line profile - column with highest partial erasure

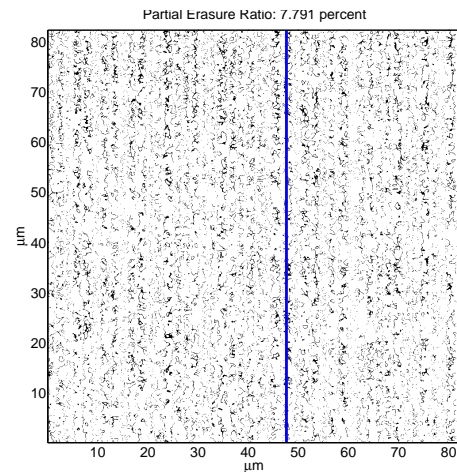


(d) FFT of the image after partially erased pixels are replaced by the mean of the surrounding pixels.

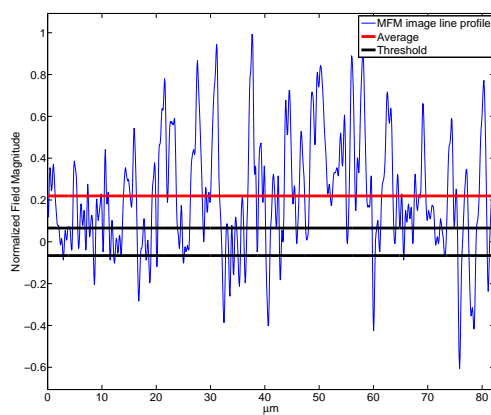
Figure 4.1: Partial erasure images - erased area.



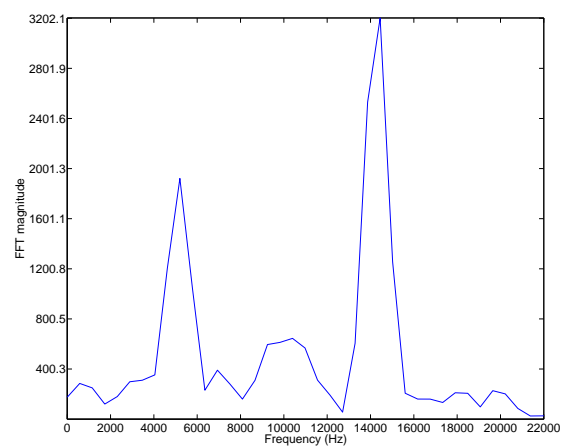
(a) MFM image - partially erased area



(b) Potential areas of partial erasure

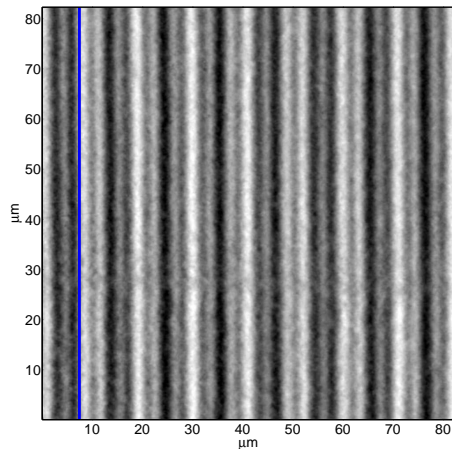


(c) Line profile - column with highest partial erasure

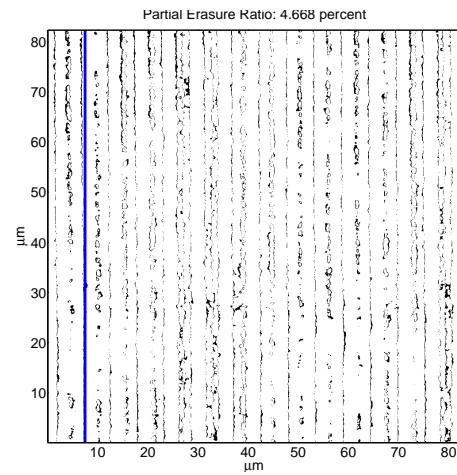


(d) FFT of the image after partially erased pixels are replaced by the mean of the surrounding pixels.

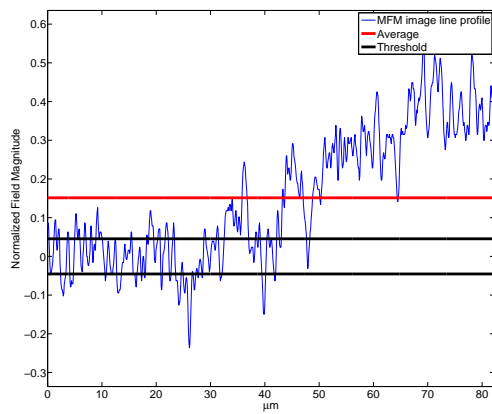
Figure 4.2: Partial erasure images - partially erased area.



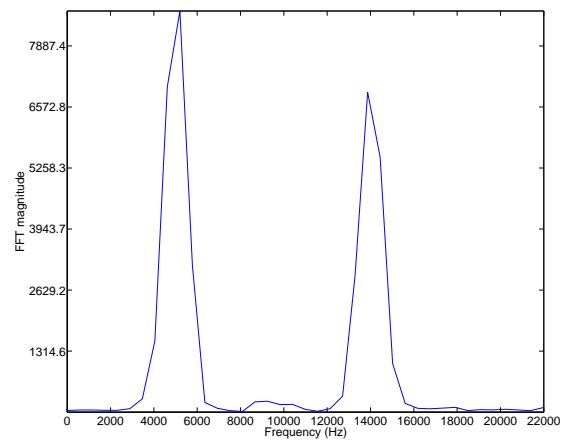
(a) MFM image - strong signal area



(b) Potential areas of partial erasure



(c) Line profile - column with highest partial erasure



(d) FFT of the image after partially erased pixels are replaced by the mean of the surrounding pixels.

Figure 4.3: Partial erasure images - strong signal area.

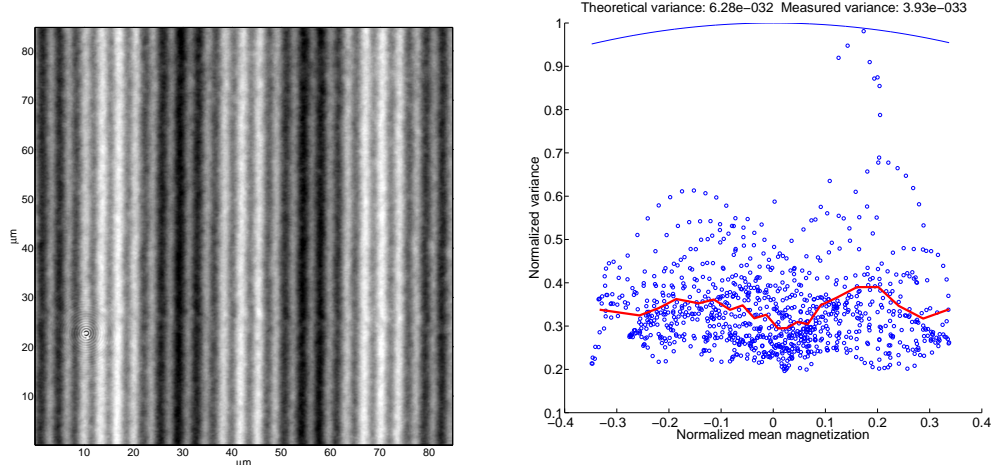
erasure, they provide a motivation for a more careful micromagnetic analysis to confirm or deny the results. In terms of signal recovery, partial erasure may be a significant factor when designing any sort of channel model for the purposes of recovering an erased or distorted signal. The FFT data for Fig. 4.1(d) shows no strong evidence of the written signals, but does show a feature that arises frequently in the multi-tone erased MFM data, a prominent peak at approximately 10 kHz . The FFT data in 4.2(d) shows strong peaks at the written frequencies, as does the MFM image in Fig. 4.3(d). This FFT data is discussed further in Subsection 4.2.2, where it is compared to raw MFM FFT data.

4.1.3 Noise Analysis

In this section, the theory of noise presented in the previous section is compared with empirical MFM measurements. First, the experimental setup including data collection and transformation techniques is presented. Then, several MFM images and their computed noise statistics are presented with an interpretative discussion of the results.

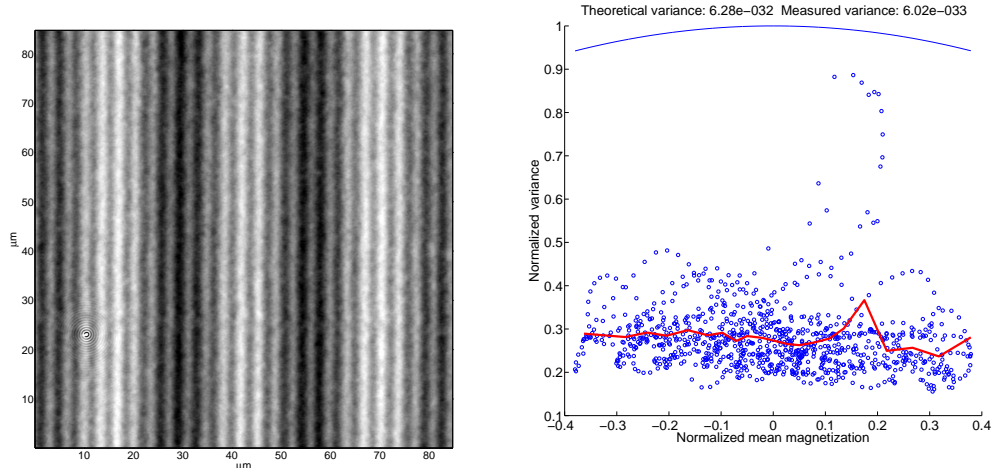
The noise theory in the previous section yielded a model for the variance of the magnetic dipole moment measured in particulate recording media. There it was determined analytically that the noise power in AC biased audio recording could effectively be considered constant. MFM has such a high resolution that it presents a unique opportunity to test this model against measurements. The steps in this experiment are as follows:

1. The set of images used consists of two images showing the sum of a 2 kHz sinusoid and a 15 kHz sinusoid on one stereo track of audio tape, and two images of that track after stereo erasure.
2. The images are each read, and the grayscale levels are converted to normalized magnetizations, as in 2.10. This is done by assuming that the mean-centered MFM grayscale output maps linearly to the sample magnetization. The actual relationship is undoubtedly more complicated than this, and provides an area for future improvements to the model.
3. Column-wise means and variances are computed for each image. It is assumed that



(a) MFM image - strong signal image 1 (b) Theoretical and measured variance versus normalized mean. Normalization terms: $6.27 \times 10^{-32}(\text{Am})^2$ and $3.92 \times 10^{-36}(\text{Am})^2$ respectively. Solid red line: means of the data.

Figure 4.4: Comparison of theoretical and measured noise statistics - strong signal 1.



(a) MFM image - strong signal image 2 (b) Theoretical and measured variance versus normalized mean. Normalization terms: $6.27 \times 10^{-32}(\text{Am})^2$ and $6.02 \times 10^{-33}(\text{Am})^2$ respectively. Solid red line: means of the data.

Figure 4.5: Comparison of theoretical and measured noise statistics - strong signal 2.

the mean magnetization is constant over each image column.

4. Theoretical values of magnetic moment variance are calculated for comparison against experiment. The computed values of normalized mean are substituted into 2.14, along with the parameters $\vec{\mu}_{particle}$, N , and \bar{P} . The latter parameters are either taken or computed from Table 2.1. The calculated experimental parameters are summarized in the list following this one.
5. The computed and theoretical values of magnetic moment variance are plotted against the normalized mean magnetization. These plots are used to determine the strength of the relationship between the data and the theoretical model.

A summary of the values used for the model parameters is:

- $\vec{\mu}_{particle} = 5.2 * 10^{-17} Am^2$, the estimated magnetic moment for a single particle.
- $N = 23.2$ particles per MFM image pixel
- $\bar{P} = 0.40$, the volumetric packing factor for audio tape.

As seen in Fig. 4.4 through Fig. 4.7, the observed variances seemingly do not follow the theoretical variance curve very closely. However if the strong signal plots are compared to the weak signal plots, to a linear factor, the strong signal plots seem to follow the theoretical curve more strongly. Notice that curvature is discernible in the theoretical plot for the strong figures. This means that the theoretical and experimental variances vary on approximately the same order. Also, a distinct looping structure is apparent in which the variance appears to follow the mean in almost inverse proportion, as predicted by the theoretical model. The experimental variance is much more widely distributed in the cases of the weak signals, as the theoretical variance appears comparatively constant on those scales. This suggests that the model may be somewhat accurate at high values of magnetization, but breaks down at very low levels of magnetization. It is clear from all of the plots that either some sort of unwanted transformation or noise exists in the data or that the model requires additional refining. Possible sources of this transformation are noise in the measurements, some non-trivial transfer function in the MFM collection technique, or some additional term that the

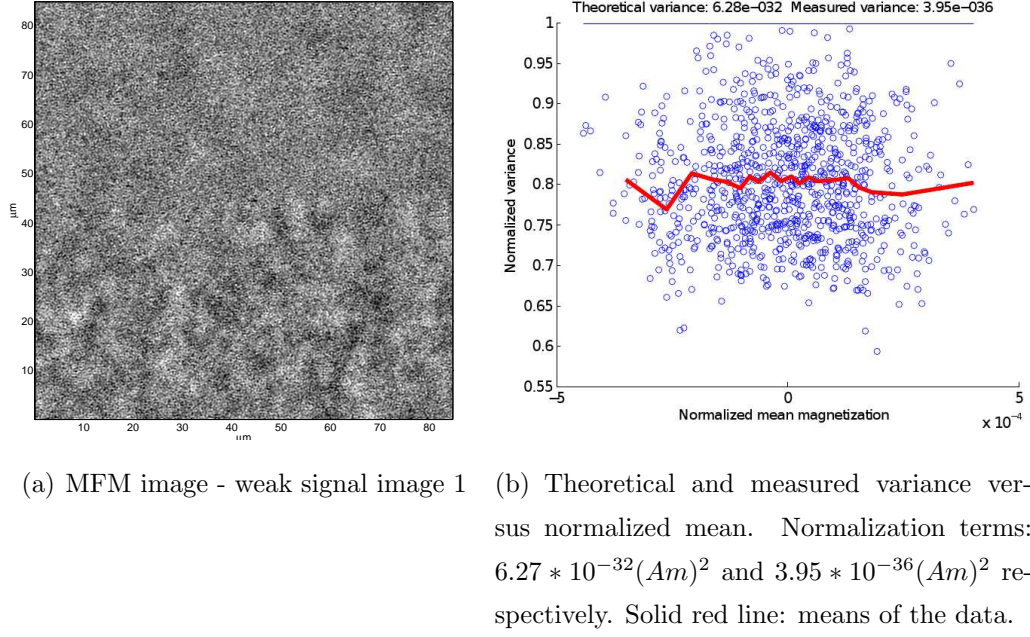


Figure 4.6: Comparison of theoretical and measured noise statistics - weak signal 1.

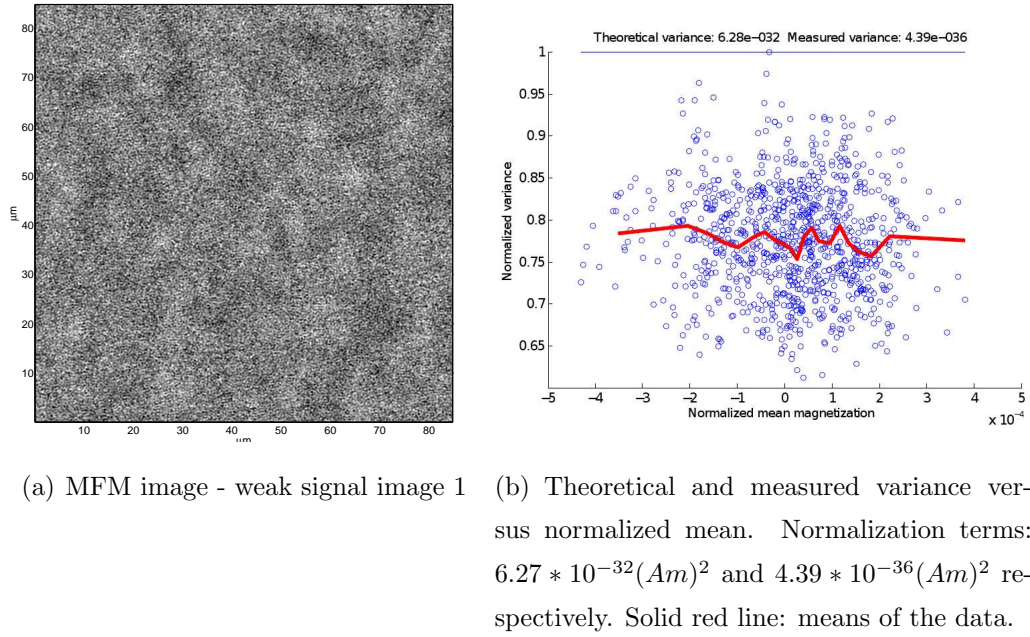


Figure 4.7: Comparison of theoretical and measured noise statistics - weak signal 2.

model is missing that becomes significant at this level of resolution. Again, future work for improving this experiment includes improving the mapping of MFM signal to sample magne-

tization as described above, and ultimately refining the model and measurement techniques until they are in agreement.

4.2 Data Recovery

This section combines the techniques described in the thesis to analyze several sets of data taken under a variety of erasure conditions. The tip response function, as described in Section 3.2.1, is applied to the raw image data and its effect on recovery is investigated. Image derotation is applied in this analysis, yielding a more accurate estimation of the frequency spectrum of the recorded signals. The erase ratio discussed in Section 4.1.1 is presented in the form of an SNR calculation. Finally, the spatial distribution of noise is investigated by correlating pairs of erased and unerased MFM images.

The signal-to-noise ratio calculation is performed for each data set by picking the strongest unerased signal from the set, computing its FFT, and using the FFT coefficients as estimates of Fourier series coefficients. The signal power is computed by summing the squared magnitude spectrum of this strong signal, according to Parseval's Theorem. This estimate of the signal spectral coefficients is then subtracted from the spectral coefficients in the erased images, and the remaining squared magnitude spectrum is summed to form an estimate of noise power. The signal-to-noise ratio is then calculated according to:

$$SNR_{dB} = 10 \log \left(\frac{P_s}{P_n} \right) \quad (4.3)$$

where P_s denotes the signal power and P_n denotes the noise power.

4.2.1 Single Tone Data

In this section, several MFM images of a single 2 *khz* sinusoid are presented, along with calculated signal-to-noise ratios. Fig. 4.8 shows the physical areas of tape from which the tone was taken. Each image contains either an erased or unerased signal. The top mono-recording track contains the unerased data, and consists of image areas A and B. The bottom mono-recording track was subjected to erasure by the tape recorder, and consists of areas C and D. A total of seven images were taken, and their SNR information is summarized in Table 4.1. A selection of three of the images and their spectrums is presented next.

Images Fig. 4.9 and Fig. 4.10 show a strong signal from area A and its spectrum. The

spectral peak is obviously well-defined at approximately 2 kHz . It is interesting to note that the signal-to-noise ratio of the image processed using the tip response function is higher than the image which has not been processed by over 2 dB . Images Fig. 4.11 and Fig. 4.12 show the images from erased area C. Unlike the image from area A, area C is much less well-defined and its spectrum is much noisier, with an SNR barely greater than zero for both the processed and unprocessed images. Unlike the strong signal, the SNR of the erased signal is greater in the unprocessed image than the processed one. This trend continues with the images from area D, Fig. 4.13 and Fig. 4.14. Area D is interesting in that while the signal is not apparent in the MFM image itself, the spectrum suggests the presence of the signal, as does the calculated SNR. Comparing the spectrum of this image with the erased signal image from area C, it is seen that the 2 kHz signal peak is much better defined and almost as prominent as the peak in the spectrum from the strong signal, area A.

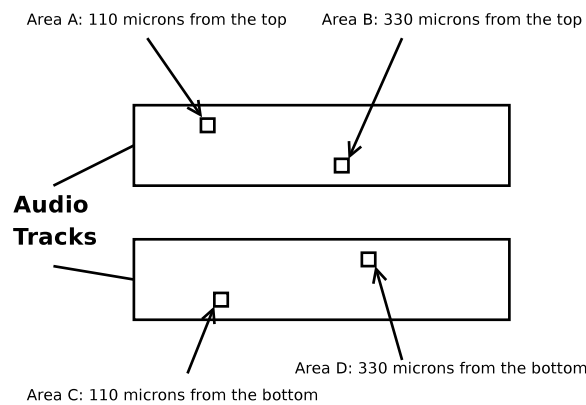


Figure 4.8: Image of audio tape layout showing the locations from which MFM data was taken. The top track is written with a 2 kHz sine wave. The bottom track was written with the same wave and then erased.

The information about all of the images in this set is summarized in Table 4.1. One major result is that in general, processing by the tip response function decreased the SNR of the detected signal. Also, there was a somewhat large variation in the SNR's calculated from the erased areas. However, these values for SNR in an erased region yield evidence that erasure performed by common recording decks may not be complete.

Image Area	Erasure Level	SNR(dB)	
		Raw Image	Tip Response Image
A1	Un erased	13.5	15.7
B1	Un erased	23.4	21.6
B2	Un erased	23.7	19.7
C1	Erased	0.283	0.213
C2	Erased	0.268	0.212
D1	Erased	1.74	1.40
D2	Erased	1.71	1.35

Table 4.1: Summary of Signal-to-Noise ratios for the single-tone data set.

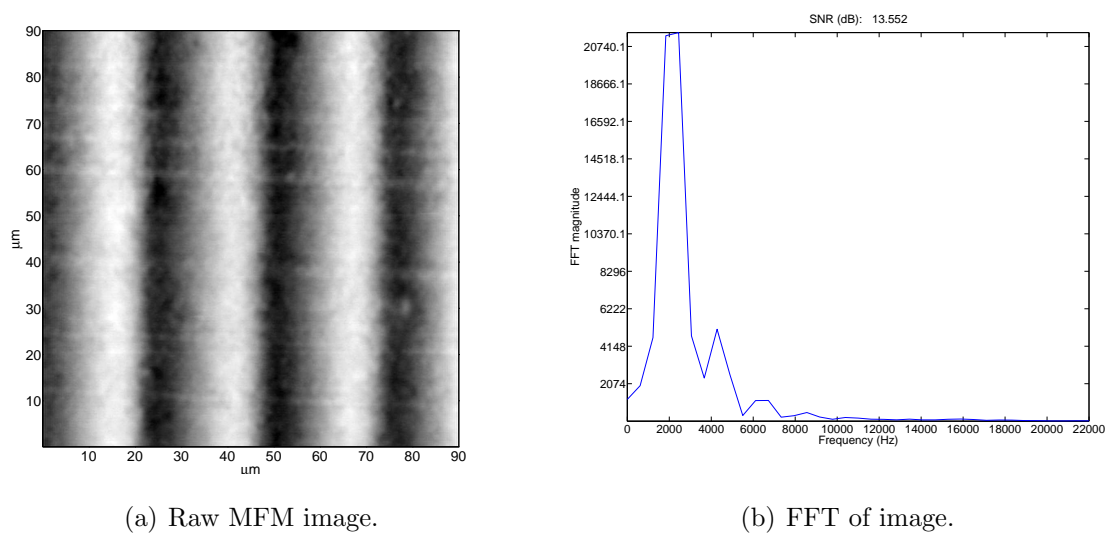
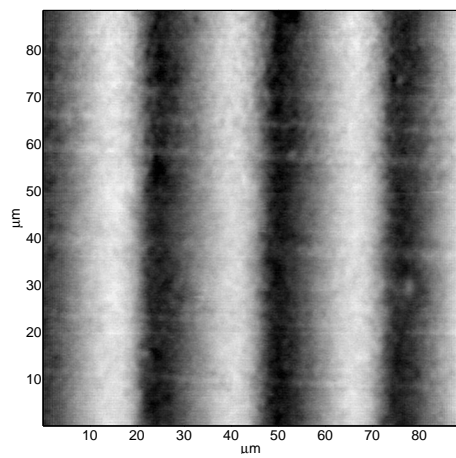
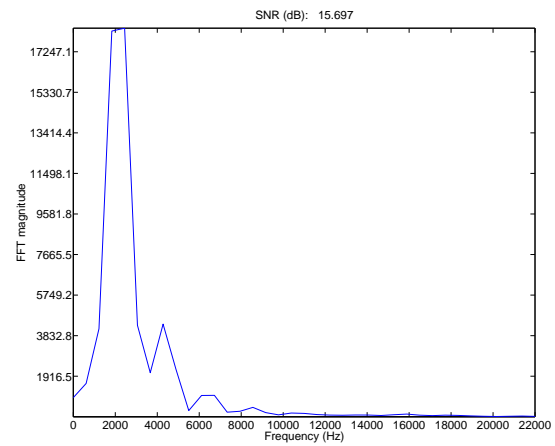


Figure 4.9: Area A - Top of unerased track - Image 1.

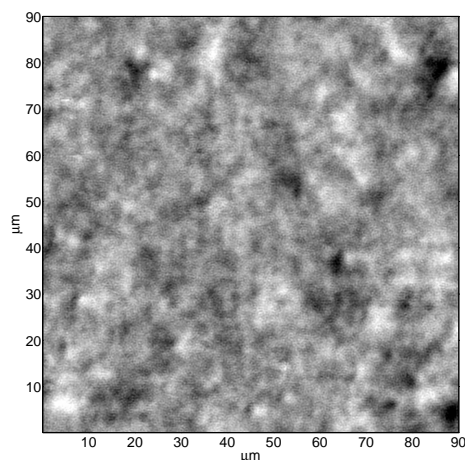


(a) MFM image processed by tip response function.

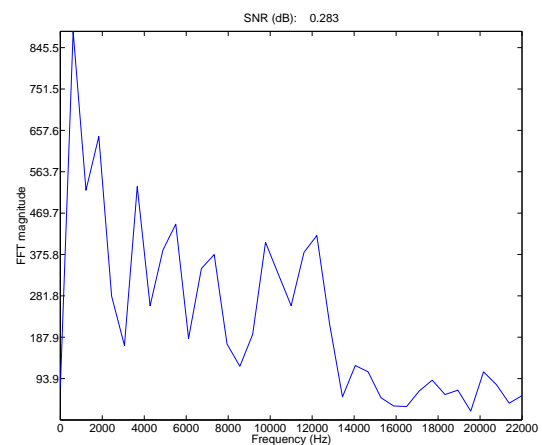


(b) FFT of image.

Figure 4.10: Area A - Top of unerased track - Image 2.

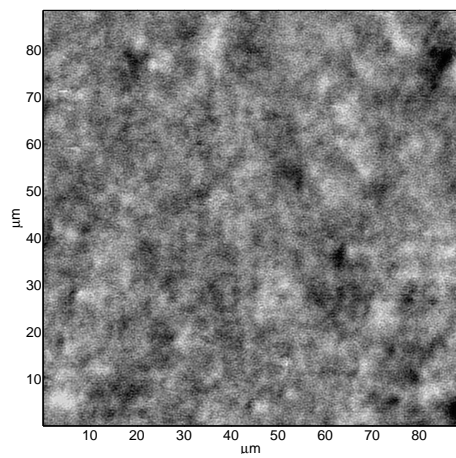


(a) Raw MFM image.

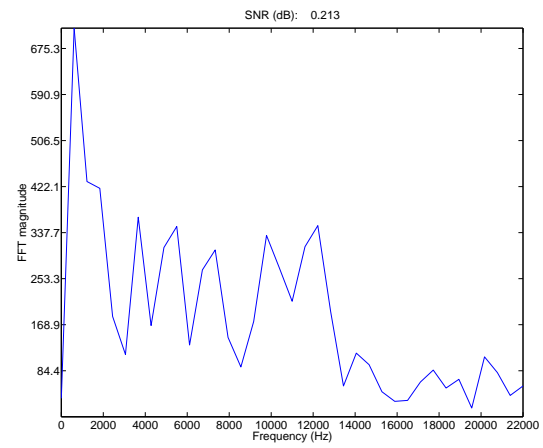


(b) FFT of image.

Figure 4.11: Area C - Top of erased track - Image 1.

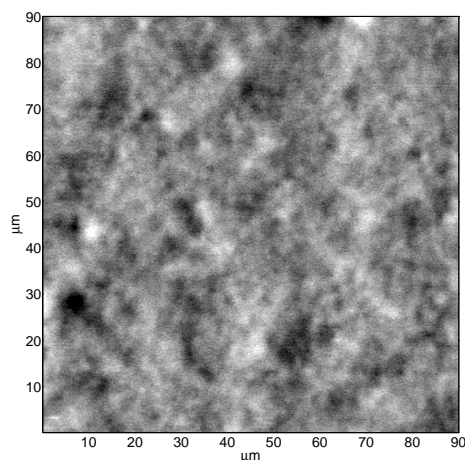


(a) MFM image processed by tip response function.

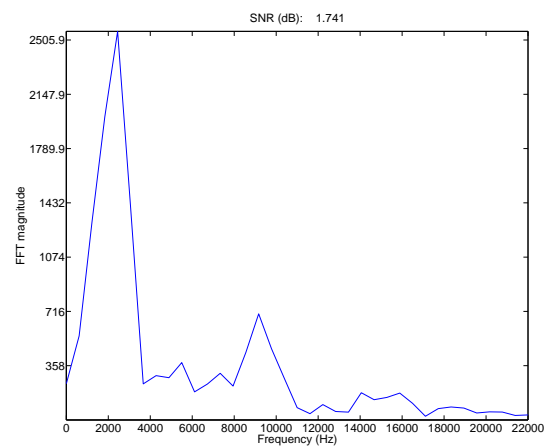


(b) FFT of image.

Figure 4.12: Area C - Top of erased track - Image 2.

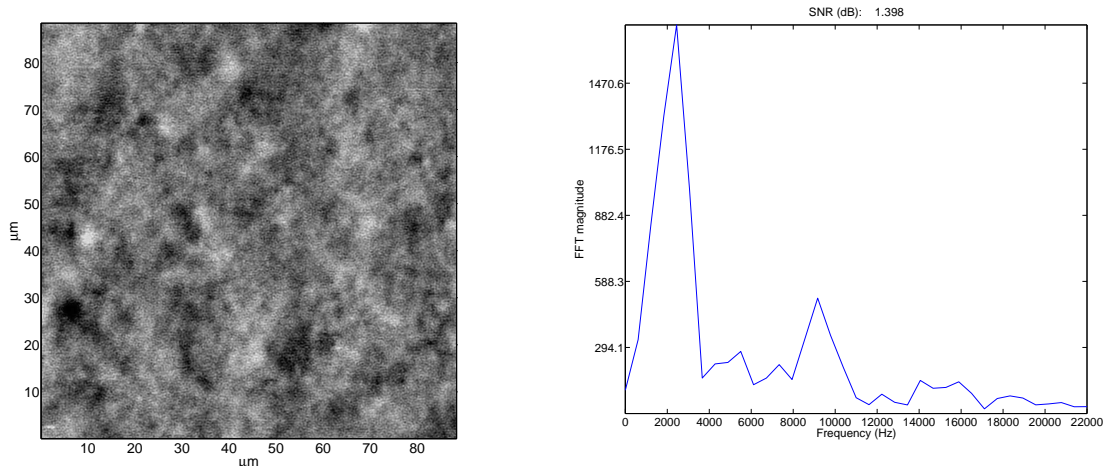


(a) Raw MFM image.



(b) FFT of image.

Figure 4.13: Area D - Bottom of erased track - Image 1.



(a) MFM image processed by tip response function.

(b) FFT of image.

Figure 4.14: Area D - Bottom of erased track - Image 2.

4.2.2 Multi-tone Data

As in the last section, MFM images of sinusoidal data are presented. However, in this case, the data consists of two sinusoids mixed together, a 5 *kHz* wave and a 14 *kHz* wave. The tape diagram is shown in Fig. 4.15. This data set consists of about twice as many images as the last, and contains images taken between the audio tracks as well as on them. The bottom mono-recorded track contains the unerased data, and the top mono-recorded track contains the erased data. The unerased data is associated with area G, while the erased data is associated with areas A, B, D, E. The middle track data is taken from areas C, H, and F. Sixteen images were taken, but only four are shown: areas A, B, G, and H. The data for the rest are summarized in Table 4.2. The images with their spectrums are presented next.

Images Fig. 4.16 and Fig. 4.17 show a strong signal from area G and its spectrum. Strong spectral peaks appear at 5 *kHz* and approximately 14 *kHz*. One notable difference between the image processed with the tip response function and the image processed without is that the 14 *kHz* peak appears noticeably higher in the processed image than in the unprocessed. This suggests that the tip response function may be more effective at enhancing higher

frequencies than lower. However this could obviously be a disadvantage if noise is distributed more in the higher frequencies than lower. While the higher frequency was enhanced, the overall SNR of the processed image is about 0.3 dB lower than the processed one. In addition to the higher frequency enhancement, some small but noticeable enhancement is present in the frequencies near zero. Comparing this spectrum with Fig. 4.3(d), we see that the two are very similar, except that the spectrum of the partial erasure processed image shows lower amplitudes for frequency components near zero. Area A, shown in Fig. 4.18 and Fig. 4.19 presents a fairly low SNR and a garbled spectrum. Comparing this spectrum with Fig. 4.1(d), no appreciable difference is noticed. Another garbled spectrum is witnessed in Area B, and again, the SNR level of the tip response processed images is lower. While neither of these images show strong peaks at either of the written frequencies, both show a peak at 10 kHz . This frequency is roughly in between the written frequencies, and could imply that some sort of “smearing” of the spectrum is occurring, such as the two frequencies heterodyning with one another. Interesting effects appear in Area H, Fig. 4.22 and Fig. 4.23, as the SNR is somewhat higher and the spectrum and image show faint signs of the 14 kHz signal. This suggests that the buffer area between tracks might contain useful information. This is also the only image in which the partial erasure processed spectrum shows a stronger signal than the raw image data. Comparing to the spectrum shown in Fig. 4.2(d), it is seen that the partial erasure processed spectrum shows the written frequencies much more clearly. Refining this partial erasure processing technique provides an interesting avenue for future work in the detection of partially erased signals.

Table 4.2 provides a summary of this data set. Unlike the previous set, none of the erased areas show a particularly high SNR. Probably the most interesting feature is the mid-track data, which yields a higher SNR than all of the erased areas. The SNR distribution is much more uniform in this data set than the last. The tip response processed images performed uniformly worse than the unprocessed images, except in the case of the mid-track data. The case in the previous set in which the strong signal yielded a higher SNR when processed with the tip function was not repeated here. The implication is that the previous case was an anomaly.

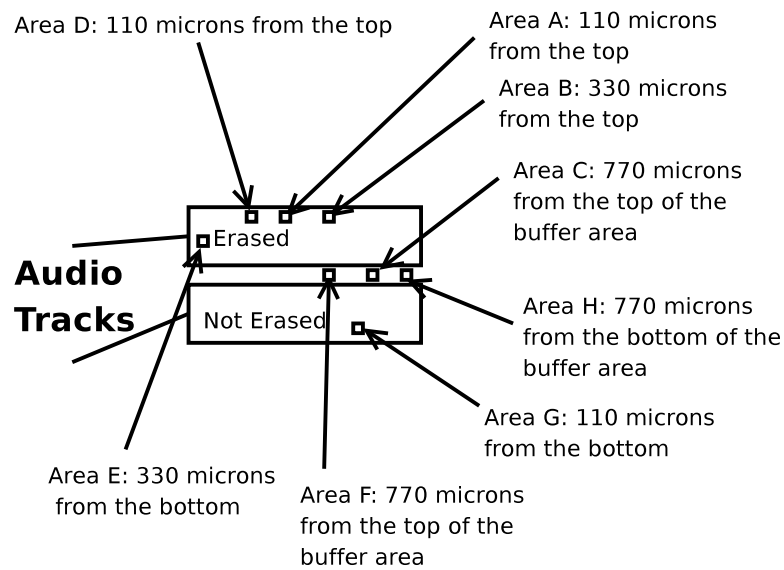


Figure 4.15: Image of audio tape layout showing the locations from which MFM data was taken. The bottom track is written with a 5 kHz and a 14 kHz sine wave. The top track was written with the same waves and then erased.

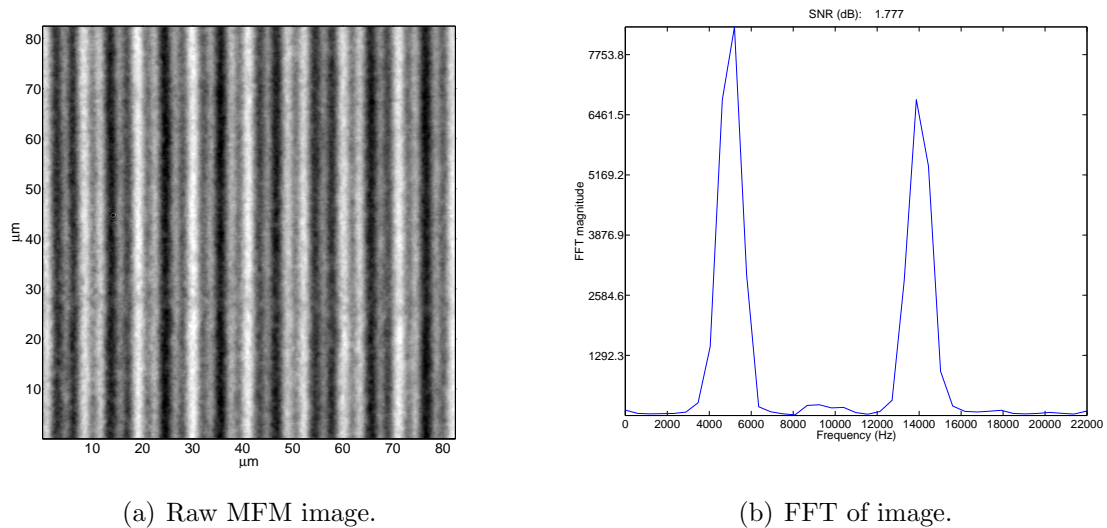
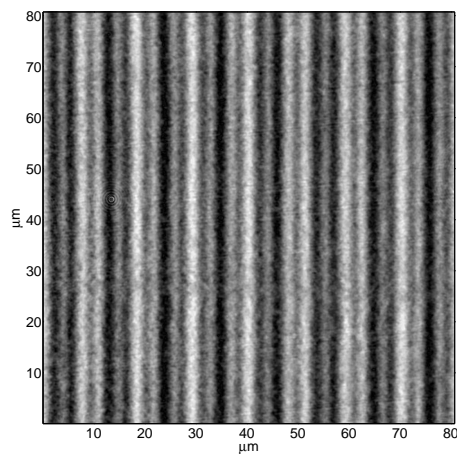
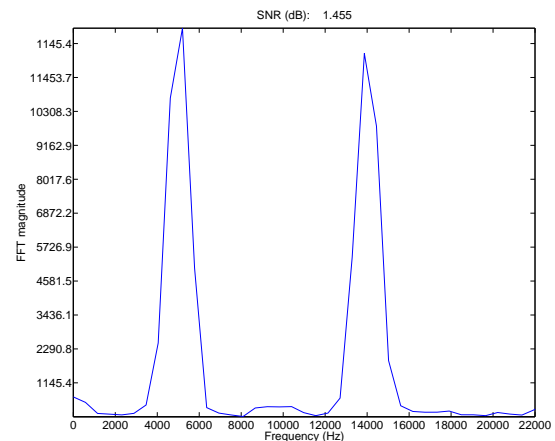


Figure 4.16: Area G - Bottom of unerased track - Image 1.

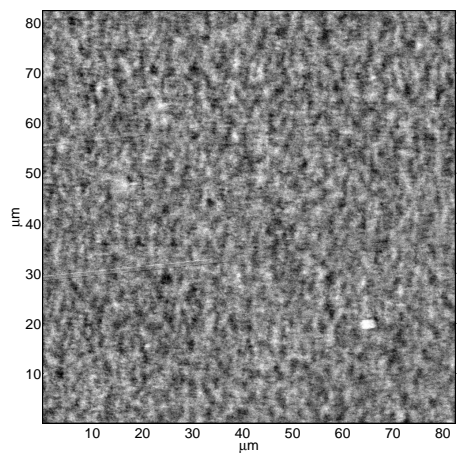


(a) MFM image processed by tip response function.

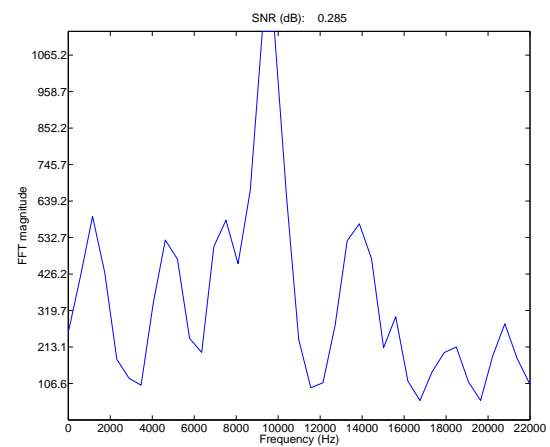


(b) FFT of image.

Figure 4.17: Area G - Bottom of unerased track - Image 2.

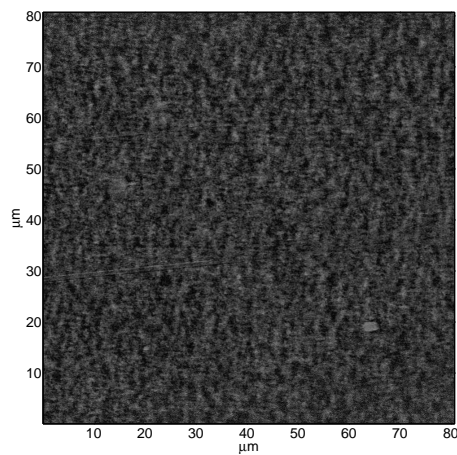


(a) Raw MFM image.

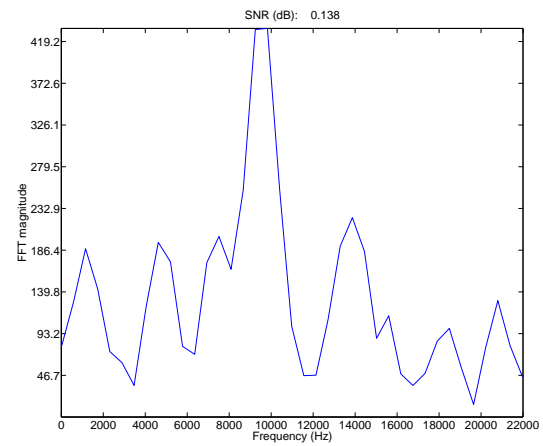


(b) FFT of image.

Figure 4.18: Area A - Top of erased track - Image 1.

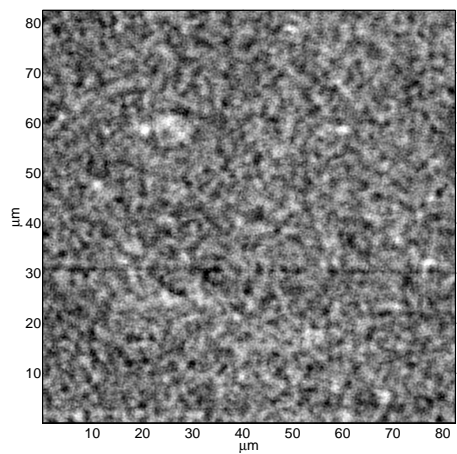


(a) MFM image processed by tip response function.

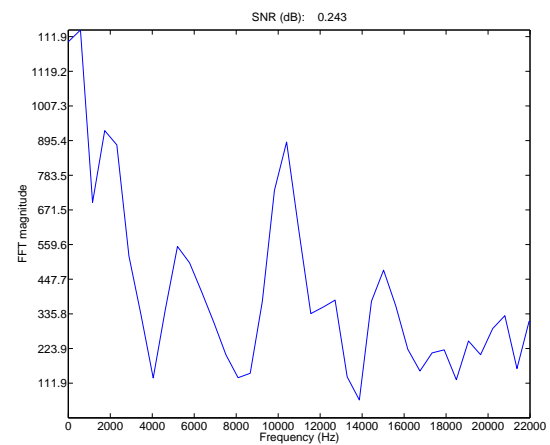


(b) FFT of image.

Figure 4.19: Area A - Top of erased track - Image 2.

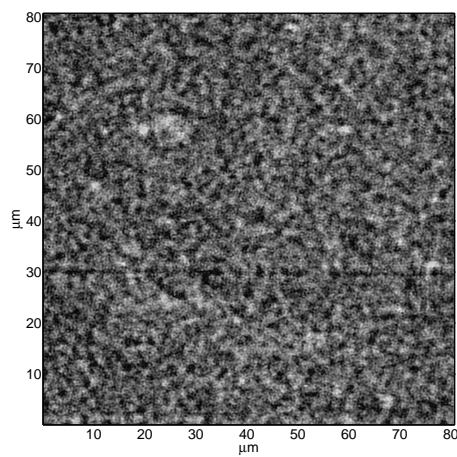


(a) Raw MFM image.

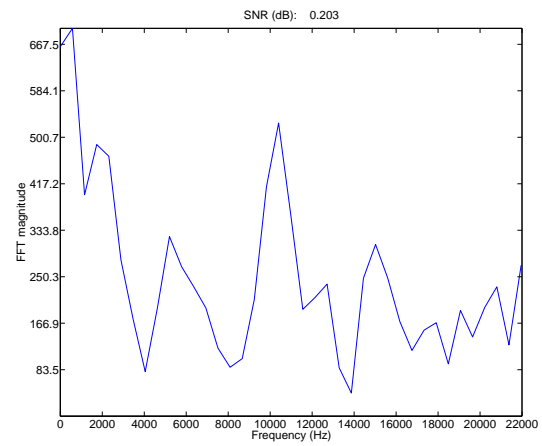


(b) FFT of image.

Figure 4.20: Area B - Top of erased track - Image 1.

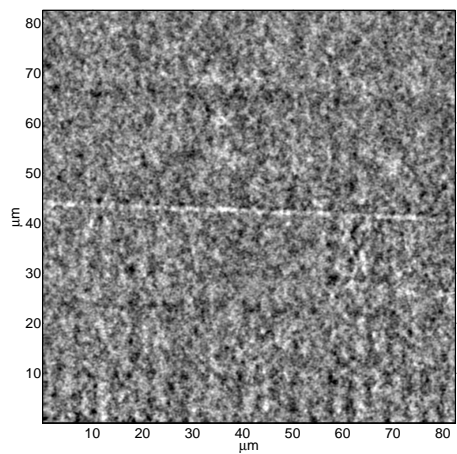


(a) MFM image processed by tip response function.

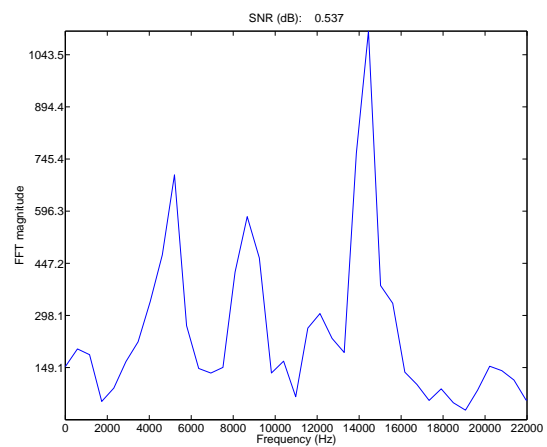


(b) FFT of image.

Figure 4.21: Area B - Top of erased track - Image 2.

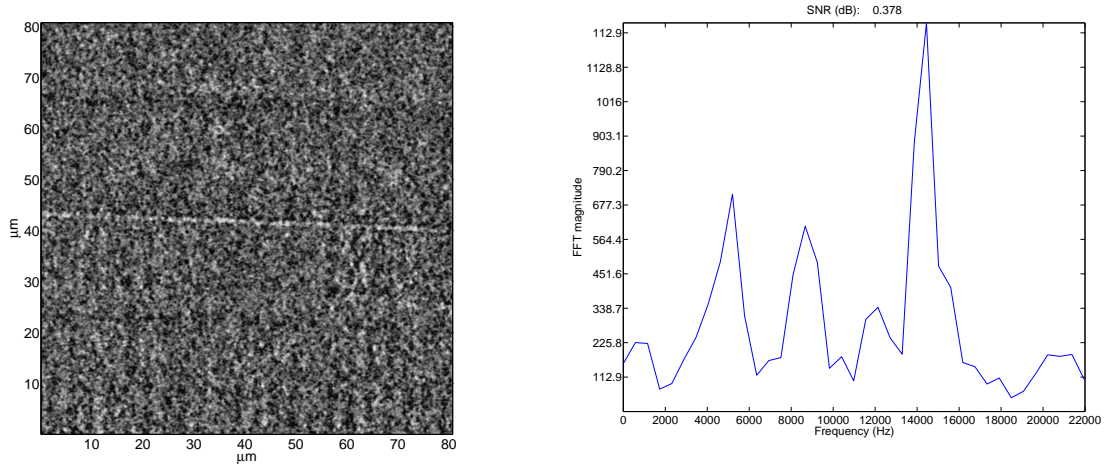


(a) Raw MFM image.



(b) FFT of image.

Figure 4.22: Area H - Buffer area - Image 1.



(a) MFM image processed by tip response function.

(b) FFT of image.

Figure 4.23: Area H - Buffer area - Image 2.

		SNR(dB)	
Image Area	Erasure Level	Raw Image	Tip Response Image
A1	Erased	0.287	0.139
A2	Erased	0.316	0.254
B1	Erased	0.246	0.206
B2	Erased	0.122	0.123
D1	Erased	0.235	0.146
D2	Erased	0.231	0.143
E1	Erased	0.111	0.082
E2	Erased	0.134	0.106
F1	Mid-track	0.133	0.087
F2	Mid-track	0.124	0.069
G1	Un erased	1.77	1.45
G2	Un erased	1.73	3.13
H1	Mid-track	0.538	0.379
H2	Mid-track	0.538	0.379
H3	Mid-track	0.538	0.379
H4	Mid-track	0.538	0.379

Table 4.2: Summary of Signal-to-Noise ratios for the multi-tone data set.

4.2.3 *In situ* Erased Data

This section differs slightly from the previous in that the samples are not erased by a tape deck, but rather modified *in situ* by the application of an electromagnet. This gives

another perspective on erasure since the exact same physical area of tape is inspected by MFM before and after modification by a magnetic field. The data consists of five images: two images of unaltered recorded tape for reference, and three images of recorded tape altered by an electromagnet. The five images are divided into two “sets”. The first set consists of three $25 \times 25 \mu m$ scans. The first image of this set is of unaltered tape, the second image is of the same imaging area altered by the electromagnet, and the third image is of the same imaging area altered a second time by the electromagnet. The second set consists of two $90 \times 90 \mu m$ scans. The first image of this set is of unaltered tape, and the second image is of the same imaging area altered by the electromagnet. The electromagnet itself was created by wrapping a wire around an iron core. The strength of the external fields created by the magnet is on the order of the coercivity of the tape, which is necessary to alter the tape’s magnetization.

Image	Erasure Level	SNR(dB)	
		Raw Image	Tip Response Image
Set 1, Image 1	Unaltered	18.6	15.4
Set 1, Image 2	Exposed once	11.2	8.86
Set 1, Image 3	Exposed twice	8.28	5.11
Set 2, Image 1	Unaltered	23.9	13.9
Set 2, Image 2	Exposed once	13.7	10.6

Table 4.3: Summary of Signal-to-Noise ratios for the electromagnet-altered data set.

The images in Figures 4.24 through 4.29 show the progression of erasure of the first sample set. The decrease in SNR’s is more gradual than in the other data sets, and the signal is never forced into a completely erased state. The trend of lower SNR’s for the tip response processed images continues uniformly in this set. The spectrums of the images do not vary appreciably, which is expected at these relatively high values of SNR. The same trends are observed in the second data set, Figures 4.30 through 4.32. The summary of SNR values are given in Table 4.3. This fine control over the erasing process motivates the study of the spatial distribution of erasure, which could be useful in defining test statistics and tests of hypothesis for the estimation of the presence of a remanent signal. For example, intuitively, if it’s shown that erasure occurs largely in “clumps”, it would suggest that discarding image features with sizes on the orders of those clumps might enhance detection of an erased signal.

More formally it could provide an estimation of the correlation length between regions of the image.

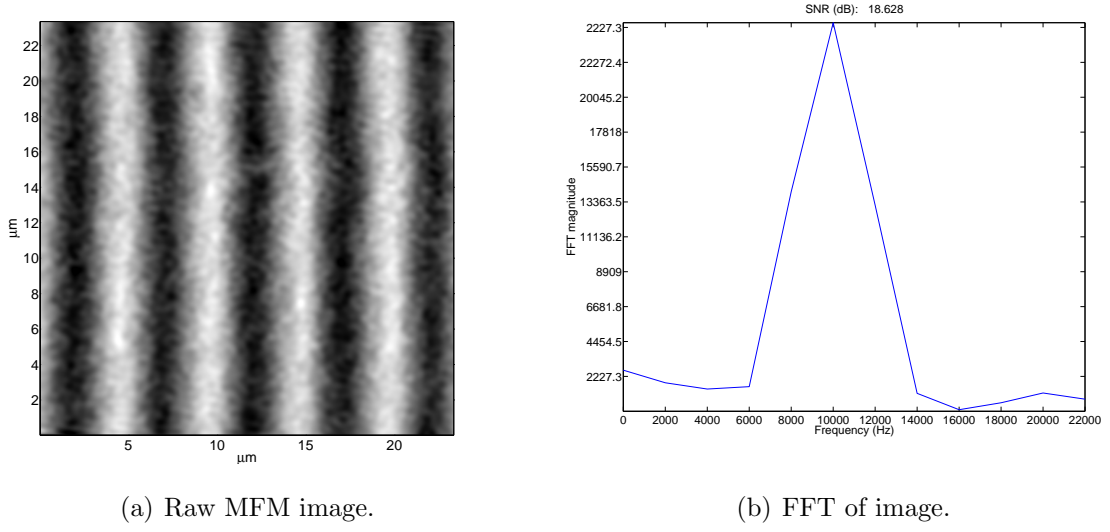


Figure 4.24: 10 kHz wave $25 \times 25 \mu\text{m}$ - Unaltered signal - Image 1.

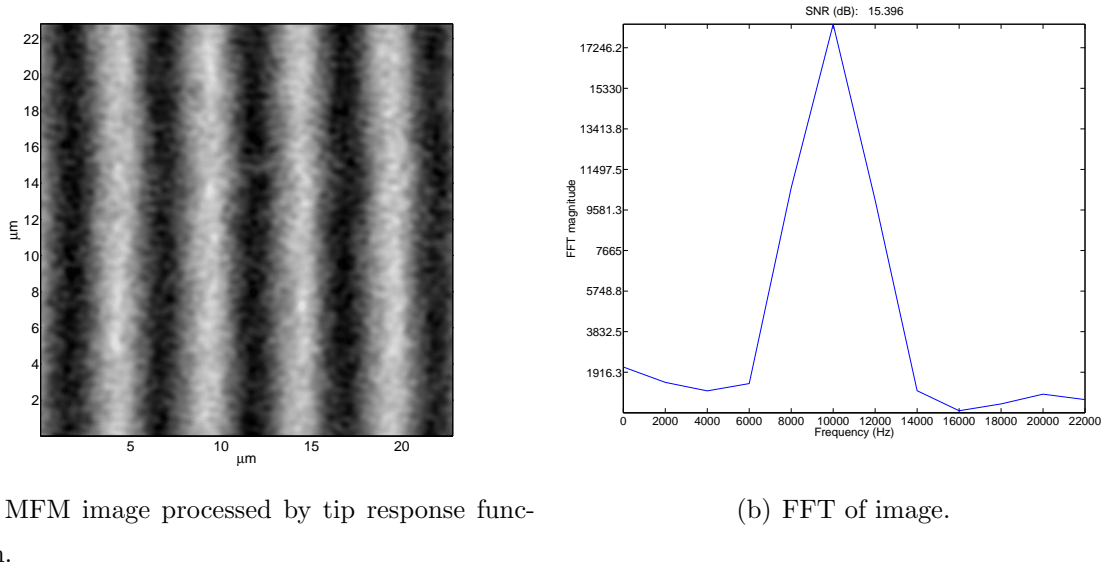
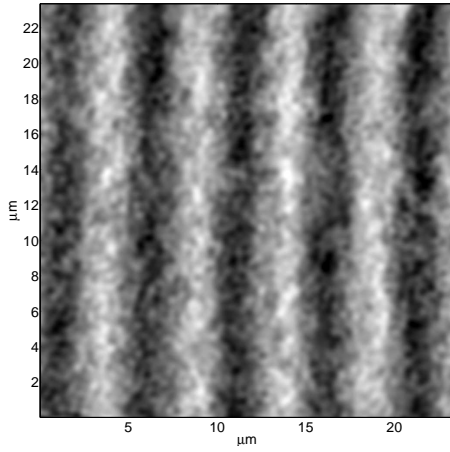
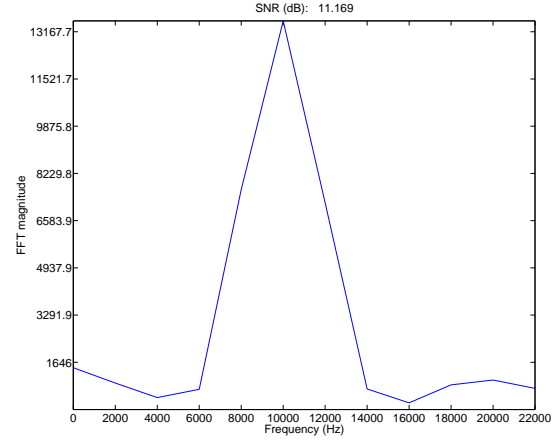


Figure 4.25: 10 kHz wave $25 \times 25 \mu\text{m}$ - Unaltered signal - Image 2.

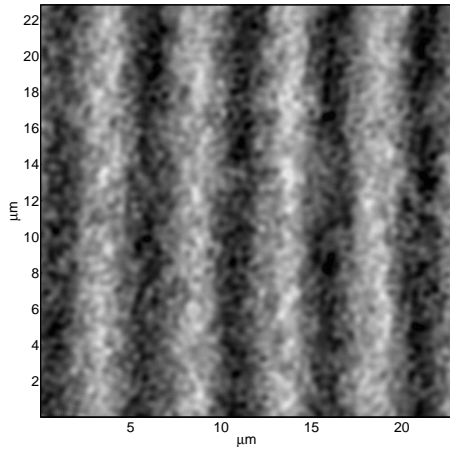
Images Fig. 4.34 through 4.36 show the result of correlating segments of the unerased reference images with the erased images. The segments are approximately $1 \mu\text{m}$ square, and



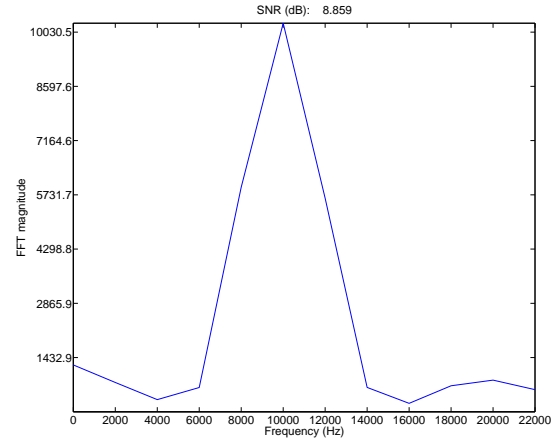
(a) Raw MFM image.



(b) FFT of image.

Figure 4.26: 10 kHz wave $25 \times 25 \mu\text{m}$ - First altered signal - Image 1.

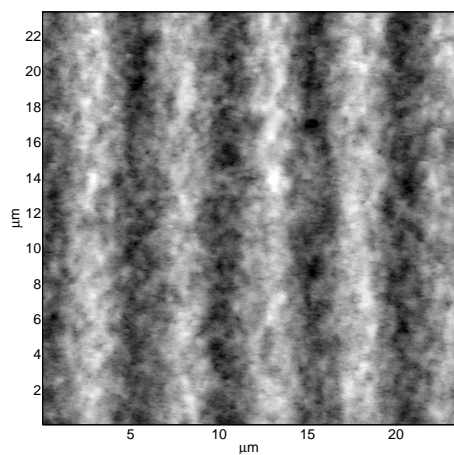
(a) MFM image processed by tip response function.



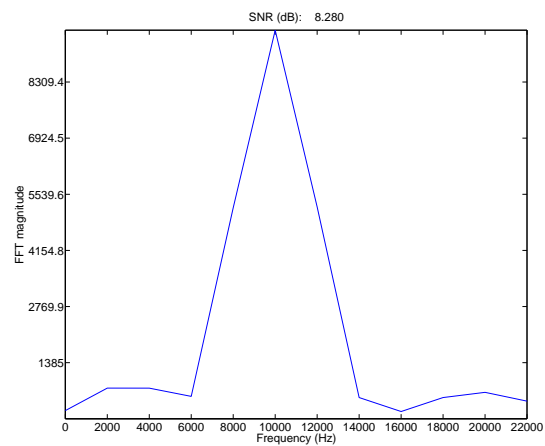
(b) FFT of image.

Figure 4.27: 10 kHz wave $25 \times 25 \mu\text{m}$ - First altered signal - Image 2.

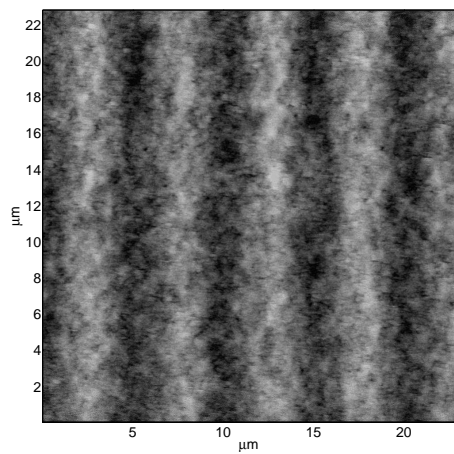
are computed after aligning two images by correlation. Alignment is necessary to compensate for slight drifts in the MFM cantilever position between sample erasures. It is often seen that areas of relatively low correlation are surrounded by areas of much higher correlation, for example in the lower left corner. This implies that diversity combining techniques may be used to detect erased signals.



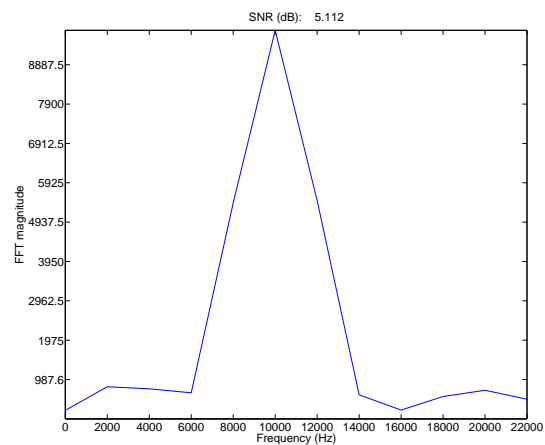
(a) Raw MFM image.



(b) FFT of image.

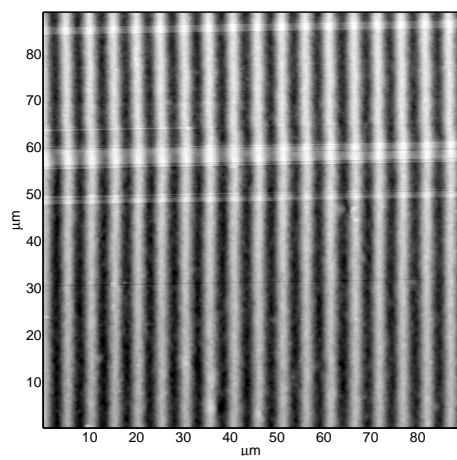
Figure 4.28: 10 kHz wave 25x25 μm - Second altered signal - Image 1.

(a) MFM image processed by tip response function.

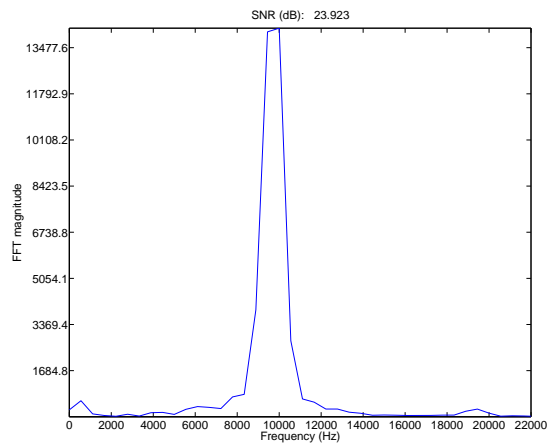


(b) FFT of image.

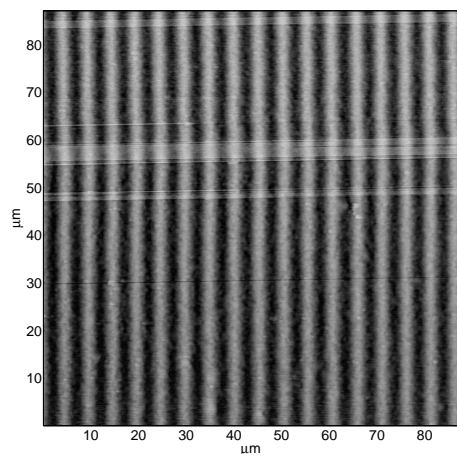
Figure 4.29: 10 kHz wave 25x25 μm - Second altered signal - Image 2.



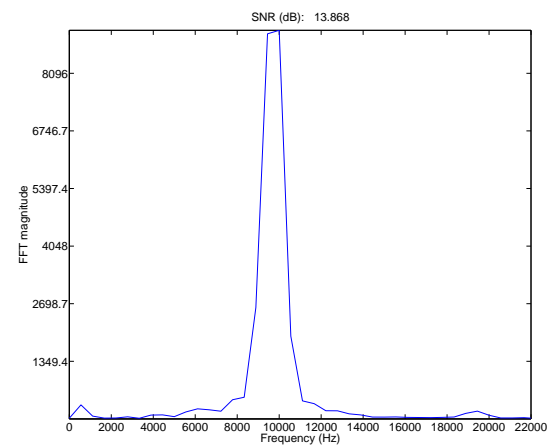
(a) Raw MFM image.



(b) FFT of image.

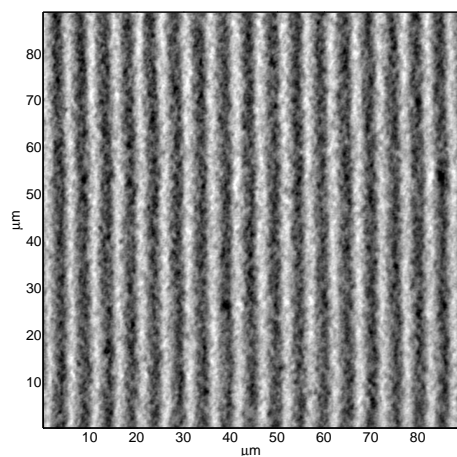
Figure 4.30: 10 kHz wave $90 \times 90 \mu m$ - Unaltered signal - Image 1.

(a) MFM image processed by tip response function.

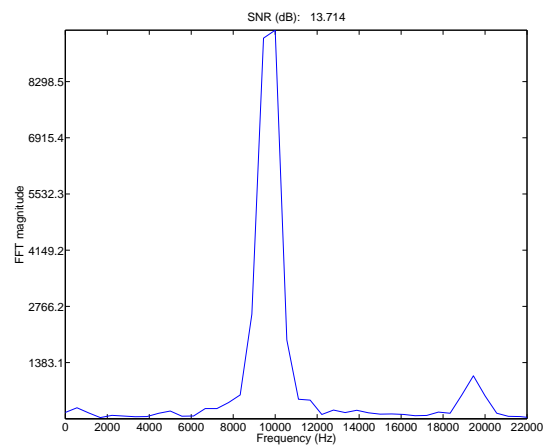


(b) FFT of image.

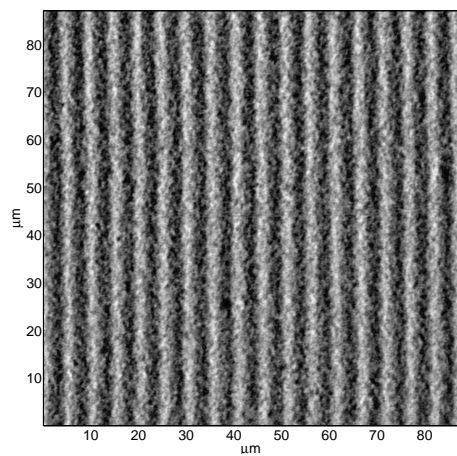
Figure 4.31: 10 kHz wave $90 \times 90 \mu m$ - Unaltered signal - Image 2.



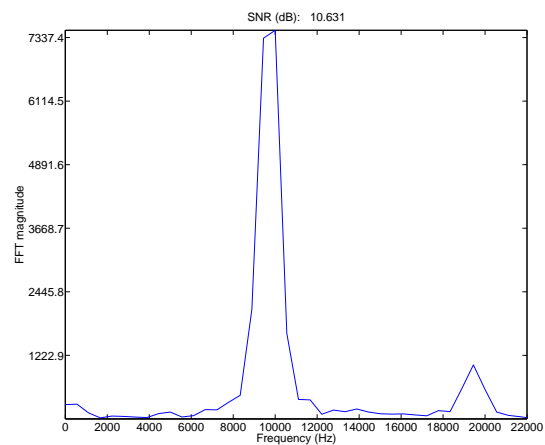
(a) Raw MFM image.



(b) FFT of image.

Figure 4.32: 10 kHz wave $90 \times 90 \mu m$ - Altered signal - Image 1.

(a) MFM image processed by tip response function.



(b) FFT of image.

Figure 4.33: 10 kHz wave $90 \times 90 \mu m$ - Altered signal - Image 2.

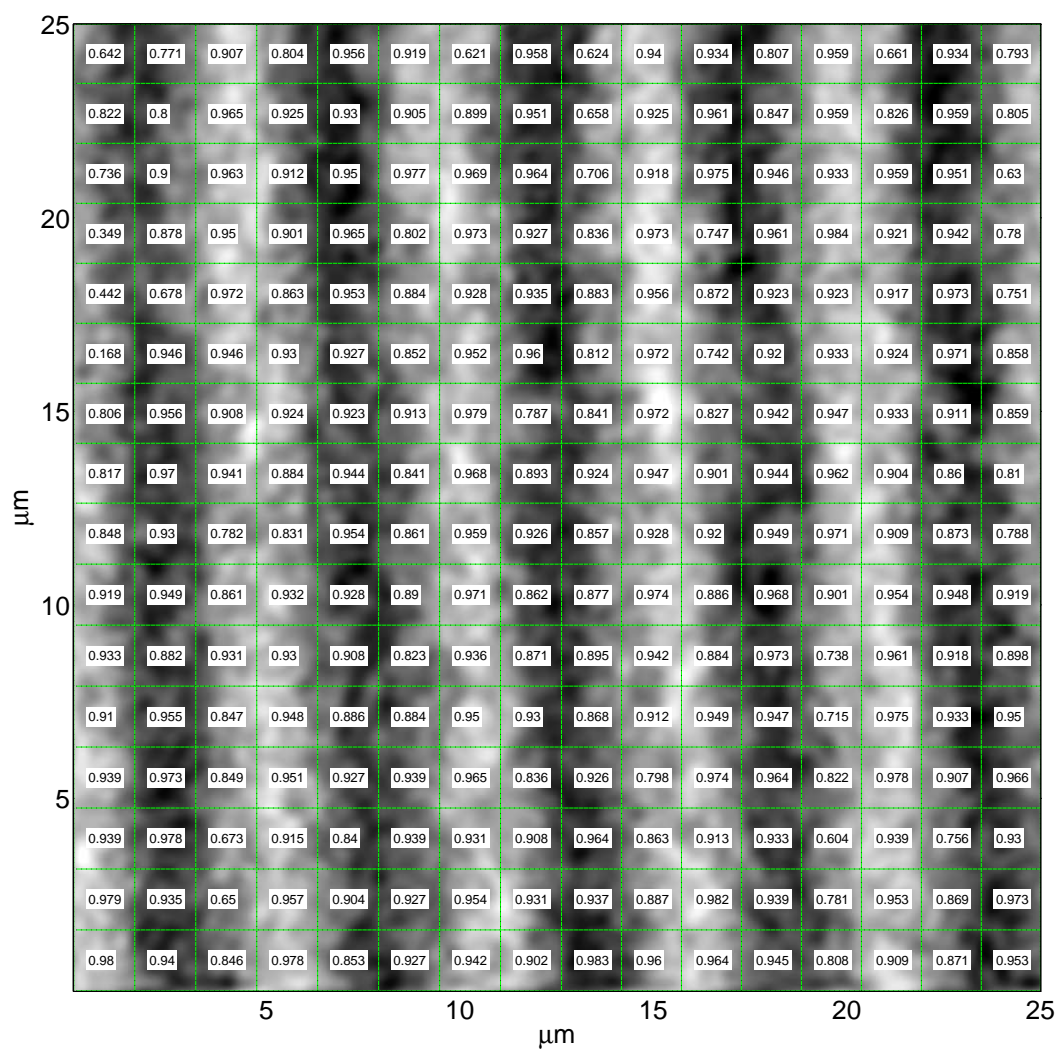


Figure 4.34: Image showing the correlation between segments of Fig. 4.24(a) and Fig. 4.26(a).

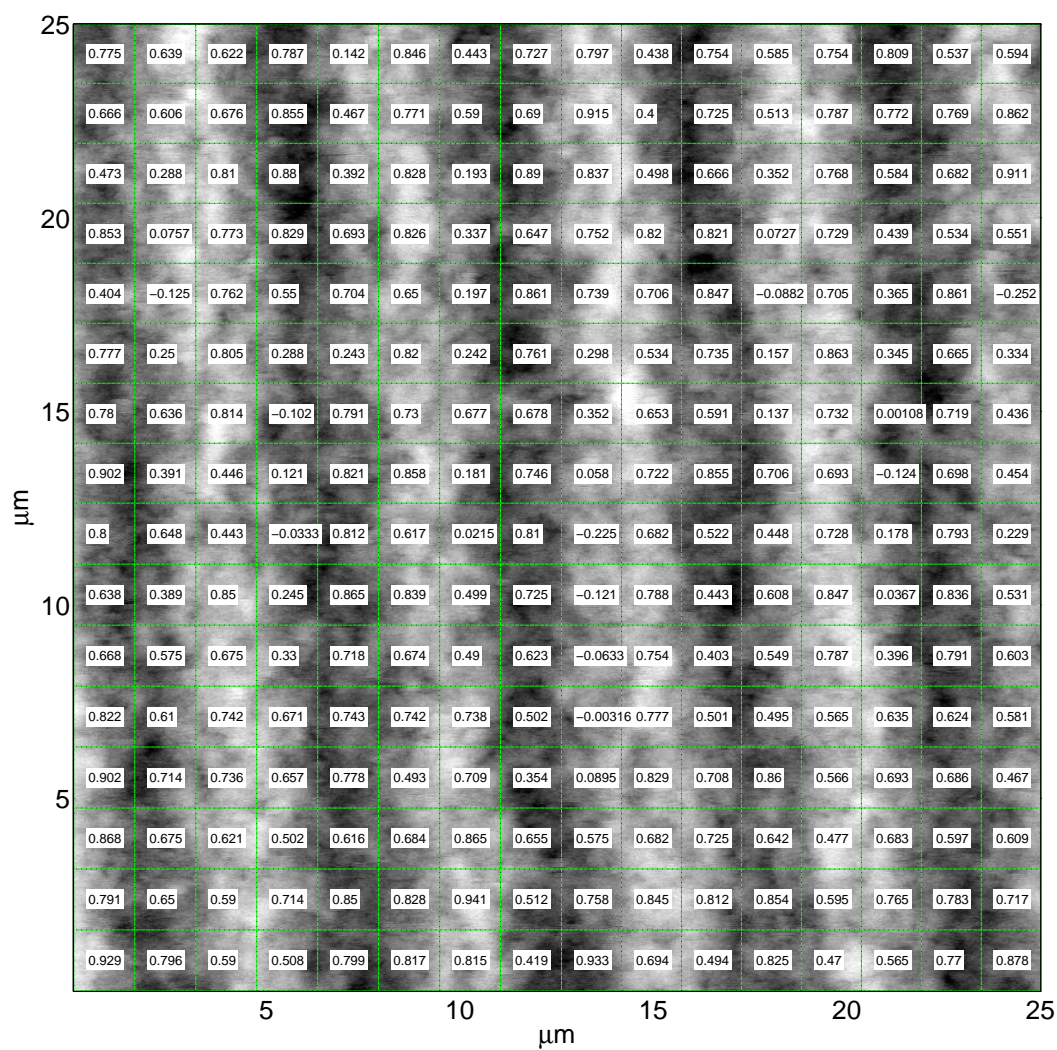


Figure 4.35: Image showing the correlation between segments of Fig. 4.24(a) and Fig. 4.28(a).

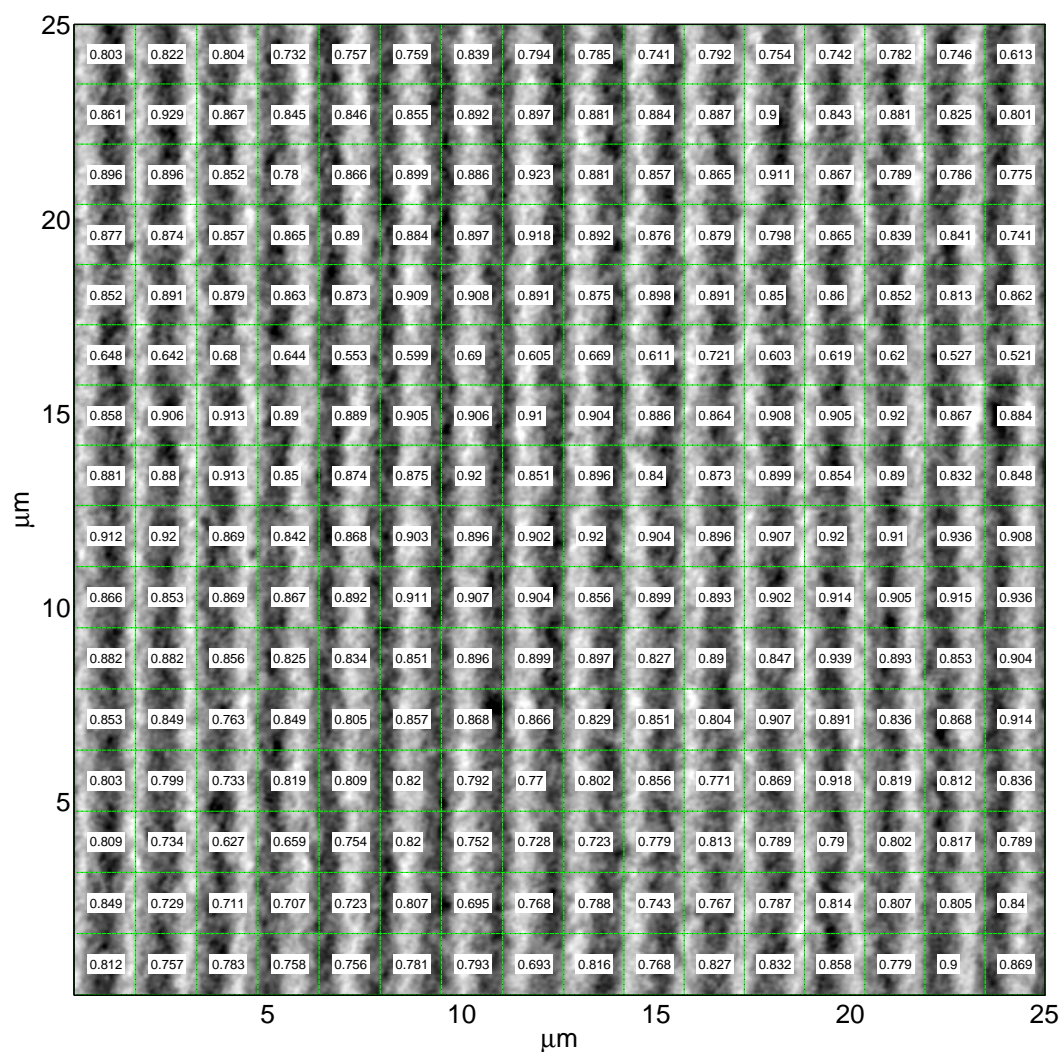


Figure 4.36: Image showing the correlation between segments of Fig. 4.30(a) and Fig. 4.32(a).

Chapter 5

Conclusion

5.1 Summary and Conclusions

The goal of this thesis was to propose and investigate a method for recovering erased data from audio cassette tapes using MFM. To achieve this, the following procedure was taken. First, a simulation of tape media and MFM response was presented to verify the experimental data. A procedure for removing the instrument-specific features from data was implemented in the Fourier domain using a tip response function. A theory of tape media noise was presented to explain the sources of signal corruption encountered when analyzing MFM data. Second, analysis was performed to compare the theoretical noise model with experimental data. This was followed by an FFT-based analysis of several MFM images, consisting of single tones and multiple tones, with and without the application of the tip response function. A subset of the MFM data was also preprocessed to reverse destructive magnetic interference. The *in situ* data images were also correlated with one another to measure the spatial distribution of erasure.

It was found through SNR calculations that significant amounts of erased signal can be present even in erased tape media. It was also found that lower frequency tones tend to be much more resistant to erasure than higher frequency, as in the case of the simultaneous writing and erasure of 2 *kHz* and 15 *kHz* tones. In this case, recovery of the 2 *kHz* tone was deemed feasible in almost all observed erased samples, while the 15 *kHz* tone was considered lost in all cases. To confirm that the recovery of the 2 *kHz* tone was legitimate and not just

an artifact of the data collection process, virgin tape media was analyzed and investigated for similar structures. It was confirmed that the 2 kHz was indeed a result of remanent signal. In another case, significant amounts of remanent signal were found in the buffer area between audio tracks. In the case of *in situ* data, evidence was found to suggest that erasure may vary significantly as one moves along the tape surface distances on the order of tens of microns, suggesting that different areas of the tape may contain different amounts of information about the erased signal. It was also found that the current implementation of the tip response function produces almost uniformly worse SNR performance compared to raw MFM data. However, the data also suggests that the tip response function enhances higher frequency data more than lower frequency, suggesting that there may be cases in which using the tip response function is desirable. Also, the tip response function may be improved by imaging a very small magnetic domain approximating an “impulse” of magnetic charge. This would give a more accurate measurement of the actual shape and size of the tip response.

The noise model presented in section 2.3.1 predicts that as the mean magnetization of the tape media tends towards zero, the variance of the recorded magnetization, and thus the measurement noise, should increase. It was found through experimental measurement that the theoretical model followed the means of experimental measurements accurately to a linear factor in the case of strongly recorded signals. The difference in observed magnetization variances as a function of magnetization mean is similar in both the experimental data and the theoretical prediction. However, the magnitude of variance predicted by the model is an order of magnitude higher than that observed in the data. This suggests that refinement of the model may be necessary, and that more data collection and comparison is necessary to confirm or deny this refinement.

5.2 Future Work

Future work involves investigating diversity combining techniques and other signal processing techniques such as principal component analysis for raising the signal-to-noise ratio of detected signals, much as partial erasure processing was used in this thesis. These tech-

niques, combined with the results of noise analysis, motivate the design of an optimal signal recovery method for MFM. Further refinement of the noise model is necessary to bring the results of experiment into agreement with theory. A more complete electromagnetic model, incorporating nonlinear particle interaction effects, would provide insight into the writing and erasure process, and allow more precise predictions to be made as to the nature of remanent information. A large amount of diverse MFM data of single tone sinusoids, multiple tone sinusoids, and more complicated waveforms at various frequencies is necessary to investigate the nature of erasure more fully, as it was found that remanent information can vary wildly across an erased audio track.

References

- [1] J. C. Mallinson, "A new theory of recording media noise," *IEEE Trans. Magn.*, vol. 27, pp. 3519–3531, July 1991.
- [2] C. D. Mee and E. D. Daniel, *Magnetic Recording Technology*, McGraw-Hill, 1996.
- [3] J. Spencer, "Interrogations and (false) confessions," <http://blog.austindefense.com/2007/10/articles/evidence-and-criminal-procedure/interrogations-and-false-confessions/>, 2007, [Online; accessed 16-April-2008].
- [4] CBS News, "Watergate tape gap still a mystery," <http://www.cbsnews.com/stories/2003/07/27/politics/main565298.shtml>, 2003, [Online; accessed 15-April-2008].
- [5] T. McNichol, "Richard nixon's last secret," http://www.wired.com/wired/archive/10.07/nixon_pr.html, 2003, [Online; accessed 16-April-2008].
- [6] D. Rugar, H.J. Mamin, P. Guethner, S. E. Lambert, J. E. Stern, I. McFadyen, and T. Yogi, "Magnetic force microscopy: general principles and application to longitudinal recording media," *J. Appl. Phys.*, vol. 68, no. 3, pp. 1169–1183, August 1990.
- [7] D. P. Pappas, A. V. Nazarov, D. Stevenson, S. Voran, M. E. Read, E. M. Gormley, J. Cash, K. Marr, and J. J. Ryan, "Second-harmonic magnetoresistive imaging to authenticate and recover data from magnetic storage media," *Journal of Electronic Image*, vol. 89, no. 11, pp. 6772–6774, Jan-Mar 2001.
- [8] R. D. Gomez, E. R. Burke, A. A. Adly, I. D. Mayergoyz, and J. A. Gorczyca, "Microscopic investigations of overwritten data," *J. Appl. Phys.*, vol. 73, no. 10, pp. 6001–6003, May 1993.
- [9] I. D. Mayergoyz, C. Tse, C. Krafft, and R. D. Gomez, "Spin-stand imaging of overwritten data and its comparison with magnetic force microscopy," *J. Appl. Phys.*, vol. 89, no. 11, pp. 6772–6774, June 2001.
- [10] T. Chang, M. Lagerquist, J-Gang Zhu, J. H. Judy, P. B. Fischer, and S. Y. Chou, "Deconvolution of magnetic force images by fourier analysis," *IEEE Trans. Magn.*, vol. 28, no. 5, pp. 3138–3140, September 1992.
- [11] T. K. Taguchi, A. Takeo, and Y. Tanaka, "Quantitative mfm study on partial erasure behavior of longitudinal recording," *IEEE Trans. Magn.*, vol. 34, no. 4, pp. 1973–1975, July 1998.

- [12] R. A. Serway and R. J. Beichner, *Physics for Scientists and Engineers*, Saunders College Publishing, 2000.
- [13] TDK, “D normal bias audio tape specification,” <http://legacyproducts.tdk.com/support/pdfs/d.pdf>, 2007, [Online; accessed 26-July-2007].
- [14] W. A. Manly, “Magnetic recording for computers,” *Byte Magazine*, vol. 1, pp. 18–28, September 1975.
- [15] T. J. Silva and H. Neal Bertram, “Magnetization fluctuations in uniformly magnetized thin-file recording media,” *IEEE Trans. Magn.*, vol. 26, no. 6, pp. 3129–3139, November 1990.
- [16] A. Roesler and J. G. Zhu, “Experimental analysis of tape noise,” *IEEE Trans. Magn.*, vol. 37, no. 4, pp. 1627–1629, July 2001.
- [17] D. Denteneer and H. Cramer, “Correlation of particle length and radius; a new model for flux noise in particulate media,” *IEEE Trans. Magn.*, vol. 26, no. 5, pp. 2110–2112, September 1990.
- [18] P. Luo and H. N. Bertram, “Experimental study of signal-dependent noise in metal particle tape,” *IEEE Trans. Magn.*, vol. 38, no. 4, pp. 1807–1813, July 2002.
- [19] P. Giljer, J.M. Sivertsen, J. H. Judy, C. S. Bhatia, M. F. Doerner, and T. Suzuki, “Magnetic recording measurements of high coercivity longitudinal media using magnetic force microscopy (mfm),” *J. Appl. Phys.*, vol. 79, no. 8, pp. 5327–5329, April 1996.
- [20] M. Alex and J. Scott, “Quantification and spatial distribution of noise in written transitions measured with magnetic force microscopy,” *IEEE Trans. Magn.*, vol. 33, no. 5, pp. 2956–2958, September 1997.
- [21] S. W. Yuan and H. N. Bertram, “Statistical data analysis of magnetic recording noise mechanisms,” *IEEE Trans. Magn.*, vol. 28, no. 1, pp. 84–92, January 1992.
- [22] A. Roesler, P. Hoang, and J. G. Zhu, “Noise due to particle distributions in metal-particle media,” *IEEE Trans. Magn.*, vol. 36, no. 6, pp. 4005–4010, November 2000.
- [23] J. W. Cross, “Scanning probe microscopy (spm),” <http://www.mobot.org/jwcross/spm/>, 2003, [Online; accessed 29-July-2007].
- [24] *µmasch*, “Spm (afm, lfm...) in biology - viruses,” <http://www.spmtips.com/bibliography/biology/viruses/>, 2004, [Online; accessed 29-July-2007].
- [25] A. A. Woodworth, *Palladium and nickel interactions with stepped 6H-Silicon carbide*, Ph.D. thesis, West Virginia University, 2005.
- [26] S. L. Tomlinson and A. L. Farley, “Micromagnetic model for magnetic force microscopy tips,” *J. Appl. Phys.*, vol. 81, no. 8, pp. 5029–5031, April 1997.

- [27] NT-MDT, “Phase of cantilever oscillations,” http://www.ntmdt.ru/SPM-Techniques/SPM-Methodology/Magnetic_Force_Microscopy_MFM/Phase_of_cantilever_oscillations/text52.html, 2007, [Online; accessed 3-July-2007].
- [28] G. R. Fowles, *Analytical Mechanics Fourth Edition*, Saunders College Publishing, 2000.
- [29] *µmasch*, “Quantitative magnetic force microscopy. calibration of mfm tip,” http://www.spmtips.com/bibliography/materials_research/mfm_calibration/, 2004, [Online; accessed 3-July-2007].
- [30] D.P. Stubbs and J. L. Alexander, “Transition lengths in magnetic recording on particulate disks,” *IEEE Trans. Magn.*, vol. MAG-22, pp. 382–384, September 1986.
- [31] R. Proksch and E. D. Dahlberg, “A numerical study of MFM response,” *J. Magn. Mag. Mater.*, vol. 104-107, no. 3, pp. 2123–2126, February 1992.
- [32] R. Madabhushi, R. D. Gomez, E. R. Burke, and I.D. Mayergoyz, “Magnetic biasing and mfm image reconstruction,” *IEEE Trans. Magn.*, vol. 32, no. 5, pp. 4147–4149, September 1996.
- [33] C-C Hsu, C. T. Miller, R. S. Indeck, J. A. O’Sullivan, and M. W. Muller, “Magnetization Estimation from MFM Images,” *IEEE Trans. Magn.*, vol. 38, no. 5, pp. 2444–2446, September 2002.
- [34] T. Sawada and K. Yoneda, “Magnetic force scanning tunneling microscope imaging of overwritten data,” *IEEE Trans. Magn.*, vol. 21, no. 5, pp. 2104–2110, September 1985.
- [35] A. Stek, S.E. Stupp, and S.B. Luitjens, “Some aspects of overwrite in thick magnetic media,” *IEEE Trans. Magn.*, vol. 32, no. 5, pp. 4055–4057, September 1996.
- [36] A. Jander, P. Dhagat, R. S. Indeck, and M. W. Muller, “Mfm observation of localized demagnetization in magnetic recordings,” *IEEE Trans. Magn.*, vol. 34, no. 4, pp. 1657–1659, July 1998.
- [37] E. T. Yen, H. J. Richter, G. Chen, and G. Rauch, “Quantitative mfm study on percolation mechanisms of longitudinal magnetic recording,” *IEEE Trans. Magn.*, vol. 33, no. 5, pp. 2701–2703, September 1997.
- [38] A. V. Oppenheim and R. W. Schaffer, *Discrete-Time Signal Processing*, Prentice-Hall Inc., 1999.
- [39] F. J. Harris, “On the use of windows for harmonic analysis with the discrete fourier transform,” *Proc. IEEE*, vol. 66, no. 1, pp. 51–83, January 1978.

A Analysis Techniques Applied to MFM Data

Periodic motion is ubiquitous in nature. A child swinging on a swingset, the rotation of the hands of a clock, and the vibration of a plucked guitar string are all examples of commonly observed periodic motion. It comes as no surprise then that specialized techniques have been developed to analyze, quantify and reduce periodic data. In this section, a technique known as the *fast Fourier transform* (FFT) is introduced which is useful in analyzing the audio signals present in MFM data.

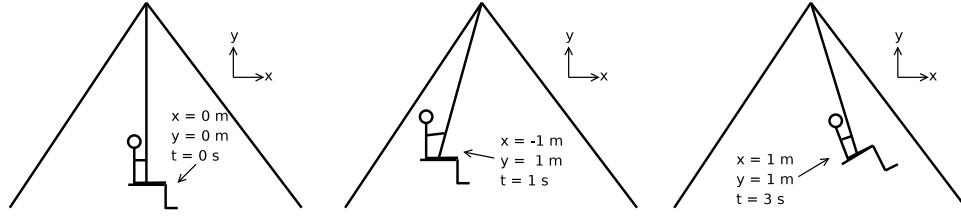


Figure .1: Child on a swing.

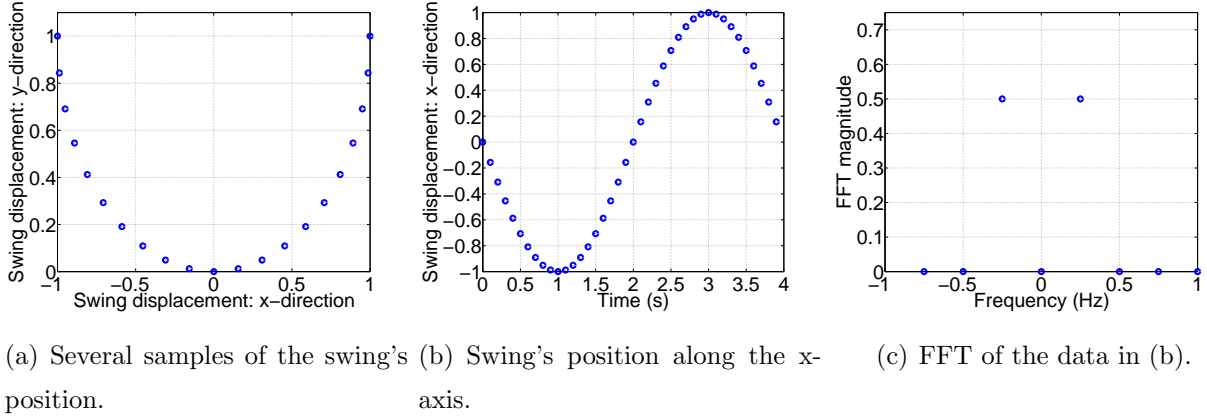


Figure .2: Swing time and frequency data.

To motivate the usage of the FFT for analyzing periodic data, an intuitive example of periodic motion is presented. Consider a child swinging on a swingset as shown in Fig. .1. Suppose we want to quantify the child's position as a function of time. Let us define a two-dimensional Cartesian coordinate system with the zero point at the swing's rest position, as shown in the figure. If we record the child's position at several instants in time and plot

them on the same graph, our graph might look like Fig. .2(a). Now, suppose that we only consider the swing's motion along the x -axis. A graph of the motion versus time might resemble Fig. .2(b).

When discussing periodic phenomena, certain concepts arise frequently, such as *amplitude*, *frequency*, and *phase offset* of the motion. In the case of the swingset, the amplitude is one meter, the frequency of the motion is $\frac{1}{4}$ hertz, and the phase offset is zero. The graph in Fig. .2(b) appears approximately sinusoidal. If we restrict the discussion to finite-length, discrete, periodic sinusoidal sequences, then a length- N sinusoidal sequence is given by:

$$y[n] = A \cos \left(\frac{2\pi kn}{N} + \phi \right) \quad (\text{A-1})$$

where A is the amplitude of the sinusoid, k is the (integer-valued) frequency of the sinusoid in hertz which takes values between 0 and $N - 1$, and ϕ is the phase offset in radians. So, a sinusoid is completely described by its amplitude, frequency, and phase offset.

Of course, not all periodic phenomena is sinusoidal. A natural question is then, can an arbitrary periodic sequence be represented in terms of sinusoidal sequences? For a discrete and finite sequence such as the swing's movement in time shown in Fig. .2(b), the answer is provided by the *discrete Fourier transform* (DFT) defined by the following expression: [38]

$$X[k] = \sum_{n=0}^{N-1} x[n] e^{-j \frac{2\pi k}{N} n} \quad (\text{A-2})$$

where N is the length of the sequence, k is the frequency of the complex exponential function in hertz, and j is the imaginary unit. While (A-2) can be used to calculate the DFT directly, the calculation is relatively slow. In practice, the DFT is computed using a more efficient algorithm, the fast Fourier transform. For the remainder of this paper, we will refer to the discrete Fourier transform as the fast Fourier transform.

Equation (A-2) can be thought of as a re-expression of the sequence $x[n]$ in terms of a sum of sinusoidal sequences. As mentioned before, these sinusoidal sequences are each completely described by their amplitude, frequency, and phase offset. To get a feel for the form of the FFT, Fig. .2(c) gives the magnitude spectrum of the swingset data given in Fig.

.2(b). This figure shows that the swingset data consists of one frequency at $\frac{1}{4}$ hertz, with the height of the data proportional to the amplitude of the swingset oscillation. While we have information about the frequency and amplitude of our data, the magnitude spectrum alone gives no information about the phase of the oscillation. For the purposes of this paper, the phase offset can be safely ignored.

Since the FFT is a decomposition of an arbitrary finite-length, discrete sequence into the sum of a set of finite, discrete sinusoidal sequences, one might ask, how many of these sinusoidal sequences are necessary to represent an arbitrary sequence? Also, how do the frequencies vary from one sinusoidal sequence to the next? The answer is that for an arbitrary sequence of length N , at most N sinusoidal sequences are required to represent the arbitrary sequence [38]. The frequency of each sinusoid is an integer multiple of the fundamental frequency $\frac{2\pi}{N}$:

$$f_k = \frac{2\pi k}{N}, k = 0, 1, \dots, N - 1 \quad (\text{A-3})$$

so the different frequencies are harmonically related. Obviously these frequency values vary between 0 and 2π .

A question that often arises is, how do the values in (A-3) map to the continuous frequency range of the signal that we have sampled? The answer is a consequence of the Nyquist Sampling Theorem, which states that to represent an arbitrary band-limited signal with maximum (sinusoidal) frequency component x hertz, the signal must be sampled at a rate of at least $f_s = 2x$ [38]. So, the expression mapping the continuous frequencies to the sampled frequencies in (A-3) is:

$$f_c[k] = f_k \frac{f_s}{2\pi}, k \leq \frac{N}{2} \quad (\text{A-4})$$

where f_s is the sampling frequency and for $k > \frac{N}{2}$, the mapping is mirrored and negative.

Notice that in Fig. .2(b), the data captures a single period of sinusoidal motion. In this case, when the data consists an exact integer number of periods of the sinusoid, the FFT data yields an exact representation of the frequency spectrum. The FFT magnitude in Fig. .2(c)

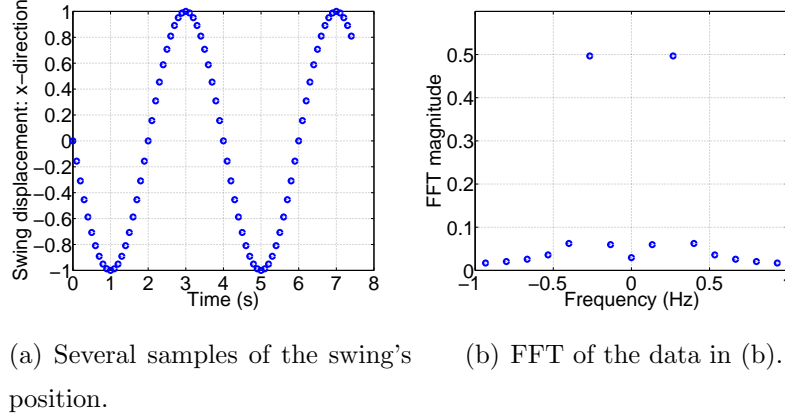


Figure .3: Swing data truncated after a non-integer number of periods.

is nonzero only at the frequency of oscillation of the swing. However, in practice, capturing data which consists only of integer number of cycles happens very rarely. In some cases it might even be impossible, such as when the data consists of a superposition of sinusoids whose frequencies are not harmonically related. What is the effect on the spectrum when the data does not contain an integer number of periods?

To investigate the effects of arbitrary truncation lengths on periodic data, we refer back to our swing example. Fig. .3(a) shows swing position data taken in the x -dimension over a non-integer number of periods and its corresponding FFT. Notice how the sinusoid is “clipped” at the end of the data on a non-zero value. Again, this is a very realistic data collection scenario since in general, we won’t be able to truncate the data as precisely as shown in Fig. .2(b). The effect of this clipping is that the spectrum is now non-zero at several points around the true frequency, as shown in Fig. .3(b). The maximum magnitude does not even occur at the true frequency! This “smearing” of the frequency spectrum is termed *leakage*, and is an unavoidable consequence of working with sampled, truncated data.

A technique known as *windowing* exists to mitigate the effect of leakage. Windowing involves multiplying the original signal by a function which tapers to zero at its edges, and possesses some nontrivial shape in between. In general, a window attempts to re-shape the frequency spectrum to more accurately represent the true frequency values at the expense of decreasing the frequency resolution [38]. To demonstrate the effects of windowing, two

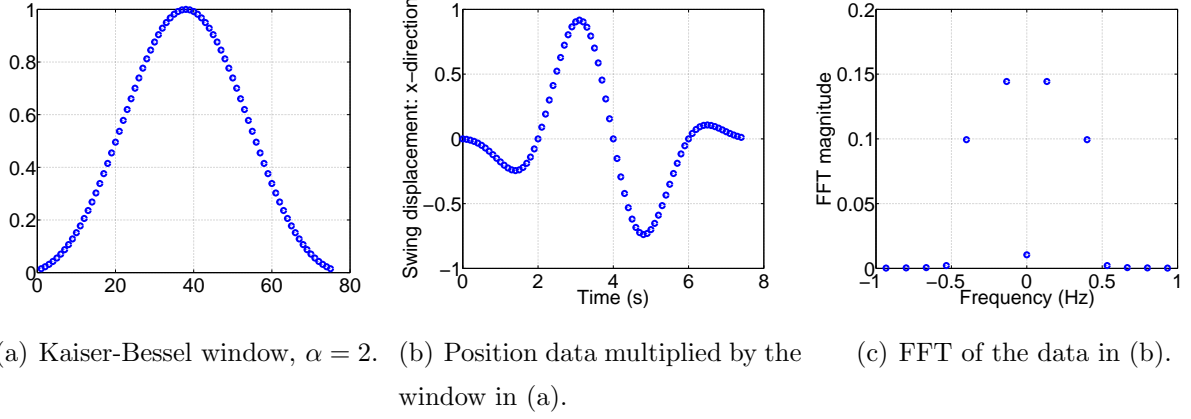


Figure .4: Kaiser-Bessel window applied to swing data in Fig. .3

windows will now be applied to our data and their effects discussed.

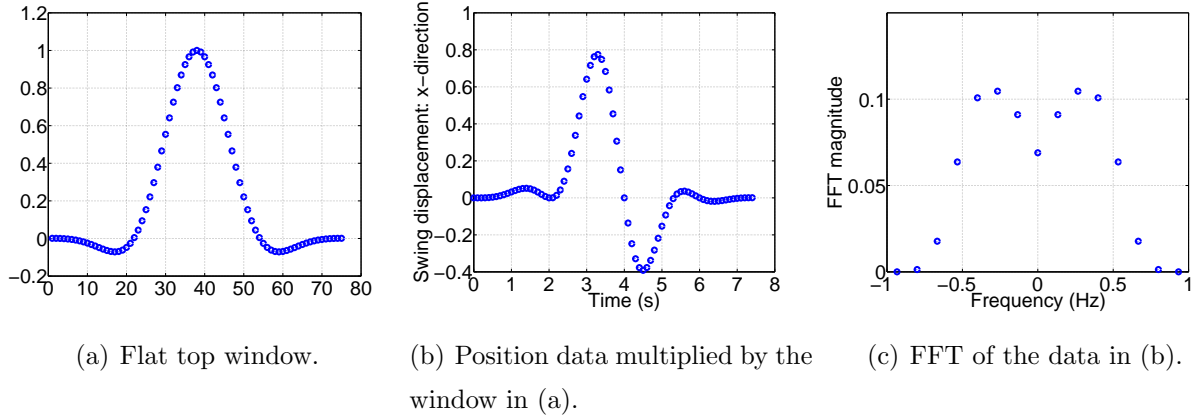


Figure .5: Flat top window applied to swing data in Fig. .3

The two windows applied to our data are the Kaiser-Bessel window and the Flat top window, as shown in Fig. .4(a) and Fig. .5(a) respectively. First, notice the effects of the windows on the original data sample, shown in Fig. .4(b) and Fig. .5(b), respectively. In both cases, the data is tapered to fall to zero at its edges. This is the reason the frequency resolution of the FFT is reduced, since the sample is essentially shortened. Now notice the effect on the spectrums. The Kaiser-Bessel window has caused the higher frequency spectral data to fall to zero, while the spectral data around the true frequency is widened, as shown in Fig. .4(c). A similar effect is observed as a result of application of the Flat top window,

as seen in Fig. .5(c), but the widening about the true frequency is even larger.

The selection of an appropriate window to apply to data is largely dependent on the nature of the data. Since the data in this thesis is sinusoidal in nature, the Kaiser-Bessel window was applied to all data prior to application of the FFT. The reason for this is that this window reduces sidelobe levels with minimal signal energy loss compared to other common windows. For example, Harris [39] found that for window parameter $\alpha = 2.0$, the signal attenuation was approximately 3 decibels, with a maximum sidelobe level of -50 decibels. This is useful for detecting sinusoidal tones with low signal-to-noise ratio while reducing leakage.